geologica acta

Citation: Molins-Vigatà, J., Blanch, X., Martín-Banda, R., García-Sellés, D., Gómez-Novell, O., García-Mayordomo, J., Insua-Arévalo, J.M., Ortuño, M., 2026. Digital surface models derived from historical aerial imagery in highly anthropized areas applied to active fault studies (eastern Betics, Spain). Geologica Acta, 24.5, 1-22. DOI: 10.1344/GeologicaActa2026.24.5 Online ISSN: 1696-5728

Digital surface models derived from historical aerial imagery in highly anthropized areas applied to active fault studies (eastern Betics, Spain)

Júlia Molins-Vigatà[1] Xabier Blanch[2] Raquel Martín-Banda[3] David García-Sellés[1] Octavi Gómez-Novell[3] Julián García-Mayordomo[3] Juan Miguel Insua-Arévalo[4] María Ortuño[1]

[1]Departament de Dinàmica de la Terra i de l'Oceà, GRC RISKNAT, UB-Geomodels, Facultat de Ciències de la Terra, Universitat de Barcelona
Martí i Franquès s/n, 08028 Barcelona, Spain. Molins-Vigatà E-mail: jmolinsvigata@ub.edu, García-Sellés E-mail: dgarcia@ub.edu, Ortuño E-mail: maria.ortuno@ub.edu

[2]Department of Civil and Environmental Engineering, Universitat Politècnica de Catalunya
08034 Barcelona, Spain. E-mail: xabier.blanch@upc.edu

[3]Instituto Geológico y Minero de España (IGME), CSIC
28760, Madrid, Spain. Martín-Banda E-mail: r.martin@igme.es, Gómez-Novell E-mail: ogomez.novell@igme.es, García-Mayordomo E-mail: julian.garcia@igme.es

[4]Departamento Geodinámica, Estratigrafía y Paleontología, Universidad Complutense de Madrid
28040 Madrid, Spain. E-mail: insuarev@geo.ucm.es

ABSTRACT

Landform recognition and surface analysis are critical in geomorphological and morphotectonic studies. In particular, the detailed study of the surface expression of active faults is essential for their characterization as seismic sources in fault-based seismic hazard models. However, increasing anthropogenic action has profoundly altered the natural landscape, degrading or erasing tectonic landforms, and limiting the accurate characterization of active faults in many regions worldwide. A paradigmatic example is the southeastern Iberian Peninsula, where extensive agricultural development over last decades has completely transformed the natural landscape. To address this limitation, we produced three historical Digital Surface Models (DSMs) using historical aerial imagery across two active faults in the Betic Cordillera: the Palomares and Llano del Águila faults. Two DSMs were generated for the Palomares Fault (one from the American B-series Flight, 1956–1957, and one from the Interministerial Flight, 1973–1986), and one DSM was generated for the Llano del Águila Fault from the Interministerial Flight, all with a spatial resolution of 2 × 2 m. We introduce Surface Roughness as a new diagnostic metric to assess quality and to identify model artifacts, while DEM of Difference analyses were used to quantify elevation changes and assess the consistency of the reconstructed surfaces. Rather than focusing solely on absolute geolocation accuracy, our approach emphasizes evaluating the reliability of the historical surface reconstruction. This methodology highlights the potential of historical aerial imagery to enhance active fault characterization and near-fault morphotectonic analyses in landscapes heavily modified by anthropogenic activity.

KEYWORDS **Photogrammetry. Historical aerial imagery. Active fault studies. Surface Roughness. Anthropogenic landscape modification. Palomares Fault. Llano del Águila Fault.**

INTRODUCTION

High-quality Digital Elevation Models (DEMs) are key tools in active tectonics and morphotectonic studies. They enable the precise identification and subsequent characterization of active faults (Bramham *et al.*, 2021; Manighetti *et al.*, 2021; McCalpin *et al.*, 2023), which is a critical step in fault-based seismic hazard assessments (Field, 2015; Stirling *et al.*, 2012; Valentini *et al.*, 2017; Woessner *et al.*, 2015). Morphotectonic analyses based on DEMs further enhance our understanding of how tectonic processes shape the landscape (Bull, 2008; Burbank and Anderson, 2013). Together with paleoseismologic investigations and geochronology, these analyses support the evaluation of key fault parameters such as slip rates, slip per event, kinematics, geometry, and segmentation (McCalpin, 2009).

However, morphotectonic and paleoseismic studies are challenged by the increasing degree of anthropogenic modification. Human impact plays a major role in modifying the natural landscape and directly conditions the interpretation and feasibility of any geomorphological analysis (García-Ruiz, 2010; Llena *et al.*, 2018). In many cases, the surface expression of faults has been significantly altered or completely erased by human activity, making current DEMs inadequate for accurate fault mapping and potentially leading to an underestimation of seismic potential. This issue is particularly critical in regions with slow-moving faults, where surface expressions tend to be subtle, especially depending on the fault's kinematics or the distributed nature of deformation (McCalpin, 2009). These subtle features are often highly susceptible to erosion or removal by human intervention. In these slow-deforming regions, highly detailed morphotectonic analyses to improve seismic hazard evaluations are essential. In these regions local populations are often less prepared, because large earthquakes occur less frequently, which can lead to disproportionately high levels of damage when such events, or even low-to-moderate magnitude events occur, as documented in the Eastern Betics (SE Spain) (Elez *et al.*, 2025; Gómez-Novell *et al.*, 2020; Herrero-Barbero *et al.*, 2021; Yazdi and García-Mayordomo, 2024).

One way to overcome this limitation is by producing DEMs using historical aerial imagery. Structure from Motion photogrammetry technique has been widely used in earthquake geology, for generating high-resolution DEMs and digitizing outcrops (McCalpin *et al.*, 2023; Reitman *et al.*, 2015). For DEM generation, not only contemporary imagery, such as drone-based data can be used, but also historical aerial photographs (Lu *et al.*, 2021). These historical datasets, offer a unique window into the pre-modified landscape, providing more reliable geomorphic baselines for identifying and analyzing fault-related features that are no longer visible today.

Structure from Motion combined with Multi-View Stereo (SfM-MVS) photogrammetry is an automated and cost-effective high-resolution technique that is able to reconstruct 3D objects and surfaces from a set of 2D overlapping images of a single scene (Eltner and Sofia, 2020; James and Robson, 2012; Westoby *et al.*, 2012). Unlike traditional photogrammetry methods, SfM-MVS does not require prior knowledge of camera positions or orientations, making it highly flexible and adaptable to a wide range of applications.

Results when applying photogrammetric techniques are directly linked to the quality of input data (O'Connor *et al.*, 2017). Therefore, high-quality results can be achieved under optimal conditions including uniform lighting, adequate image overlap, and surfaces with sufficient texture variation for feature detection and matching. Results can be compared with other methodologies such as Light Detection and Ranging (LiDAR), while requiring significantly less expensive equipment and specialized training. Consequently, SfM-MVS has gained popularity in various disciplines, due to its simplicity, flexibility, and relatively low cost. As an example, SfM-MVS aerial photogrammetry has been widely used for monitoring landslides (Stumpf *et al.*, 2013) or fluvial dynamics (Dietrich, 2016) among others and, more broadly, terrestrial photogrammetry is used to assess hazards from various surface processes such as rockfalls (Blanch *et al.*, 2021; 2024) or glacier dynamics (Ioli *et al.*, 2024; Taylor *et al.*, 2023).

One of the most valuable geospatial products derived from SfM-MVS photogrammetry is the generation of DEMs with high resolution and accuracy, often at the centimetric scale (James and Robson, 2012). A single DEM offers detailed topographic information, enabling the extraction of morphometric parameters used for the preliminary identification and analysis of geomorphological features. However, its most powerful application in geosciences lies in monitoring dynamic processes through geomorphological change detection. By generating DEMs at different moments in time, DEM of Difference (DoDs) models can be generated through simple subtraction of sequential elevation surfaces, allowing for the spatial identification and quantitative characterization of areas where elevation has changed (Eltner *et al.*, 2016; Wheaton *et al.*, 2010).

Historical aerial images are widely used in photo interpretation, in geological and geomorphological mapping. They serve as a crucial resource for studying long-term landscape changes of any kind. In the Iberian Peninsula, images from the American B-series (AmB) Flight (1956-1957 American Flight (B series), n.d.) and the

Interministerial (InM) Flight (1973-1986 Interministerial Flight, s/f n.d.) have occasionally been used to generate historical DEMs for various purposes (Aguilar *et al.*, 2013; Mestre-Runge *et al.*, 2023; Pérez-Álvarez *et al.*, 2013; Picon-Cabrera *et al.*, 2020). These studies usually focus solely on geolocation accuracy and do not assess the quality of the reconstructed surface, which can exhibit distortions or artifacts.

The quality of DEMs is often evaluated using external geodetic measurements or by analyzing inter-pixel variability, with a focus on the positional accuracy of individual cells (Knuth *et al.*, 2023; Polidori and Hage, 2020). In this study, we adopt a broader definition of DEM quality that emphasizes the faithful representation of terrain morphology, free from artifacts introduced by the limitations of the input data. Here, quality does not refer solely to the absolute accuracy of each DEM cell, but rather to the ability of the DEM to reproduce the true surface without photogrammetric or instrumental artifacts. To this end, we propose the use of Surface Roughness (Smith, 2014), used in some cases to assess the quality of DEMs with image texture of the input Data (Purinton *et al.*, 2023). Surface Roughness (Hobson, 1972; McKean and Roering, 2004; Smith, 2014) or Vector Ruggedness Measure (VRM) (Sappington *et al.*, 2007) was used as a cell-by-cell metric for DEM quality assessment, as it enables the systematic detection and characterization of artifacts, and provides a robust basis for comparing the reliability of different DEMs in morphotectonic interpretation.

Additionally, to support detailed morphotectonic analysis we used DoDs as a complementary tool for quality control at a finer, site-specific working scale. The spatial consistency of DoDs, when no real terrain changes are expected between datasets, can reveal residual distortions, alignment issues, or surface noise that might otherwise go unnoticed in static DEM analyses.

The proposed approach enables the reconstruction of extensive surfaces from large image datasets, yielding high-resolution products with low positional error. Surface Roughness is incorporated as a quantitative metric to assess spatial variations in DEM quality and to support detailed morphotectonic analyses; DoDs are computed at the working scale. This methodology substantially enhances the geomorphic characterization of fault-related features by allowing their analysis as they appeared prior to major anthropogenic disturbances.

In this study, images from the AmB flight (1956–1957) and the InM flight (1973–1986) were used to generate three different Digital Surface Models (DSMs) for the Palomares Fault (PF) and Llano del Águila Fault (LLAF) areas (Fig. 1), located in the southeast of the Iberian Peninsula. Both areas are affected by strong anthropic landscape modifications, specially the LLAF, which is situated in Campo de Dalías. Campo de Dalías is one of the regions in Europe with the largest greenhouse coverage for extensive agriculture (Mendoza-Fernández *et al.*, 2021).

The generated DSMs will enable the execution of morphotectonic analyses without the widespread anthropogenic imprint that challenges such analyses with recent DEMs in the region nowadays. This will allow, for example, the identification of fault scarps, the measurement of vertical and lateral offsets, and the recognition of deposits affected by fault activity, prior to the anthropogenic modifications of the landscape. Additionally, they will facilitate the identification and verification of areas that remain unaltered, which will be of particular interest for conducting detailed studies, such as paleoseismic trenching, in the future.

STUDIED ACTIVE FAULTS

Geodynamic setting

The studied faults are located in the southern Iberian Peninsula, within the eastern sector of the Betic Cordillera, where several local kinematics environments coexist in a regional plate convergence context (Fig. 1). At present, the Nubian and Eurasian plates converge at a rate of approximately 4 to 6 mm/year (*e.g.* Echeverria *et al.*, 2013; Palano *et al.*, 2015; Portela *et al.*, 2025) with a predominant N-S to NW-SE shortening direction, mainly accommodated by the Eastern Betic Shear Zone (EBSZ) (*e.g.* Bousquet, 1979; Silva *et al.*, 1993). The compression is primarily accommodated by N-S to NE-SW oriented left-lateral strike-slip faults with a reverse component in the EBSZ and partially accommodated by NNW-SSE to WNW-ESE high-angle normal faults in the Central Betic Cordillera (Buforn *et al.*, 1988; Galindo-Zaldívar *et al.*, 2003; Marín-Lechado *et al.*, 2005; Martínez-Díaz *et al.*, 2012; Molins-Vigatà *et al.*, 2022).

This region is one of the most seismically active areas in the Iberian Peninsula (García-Mayordomo *et al.*, 2007). Despite estimated geological and geodetic fault slip rates are below 2 mm/yr (Gómez-Novell *et al.*, 2022; Martín-Banda *et al.*, 2021; Moreno, 2010; Ortuño *et al.*, 2012; Pedrera *et al.*, 2012), both instrumental and historical earthquakes have been attributed to these faults, including the PF and LLAF (Fig. 1) and consequently have caused significant damage in the past. The November 9, 1518 Vera earthquake, with intensity IEMS VII-IX and estimated Mw ~6.2, which completely destroyed the old town of Vera, has been associated with the PF (Martínez-Solares and Mezcua, 2002; Yazdi *et al.*, 2023). Similarly, the August

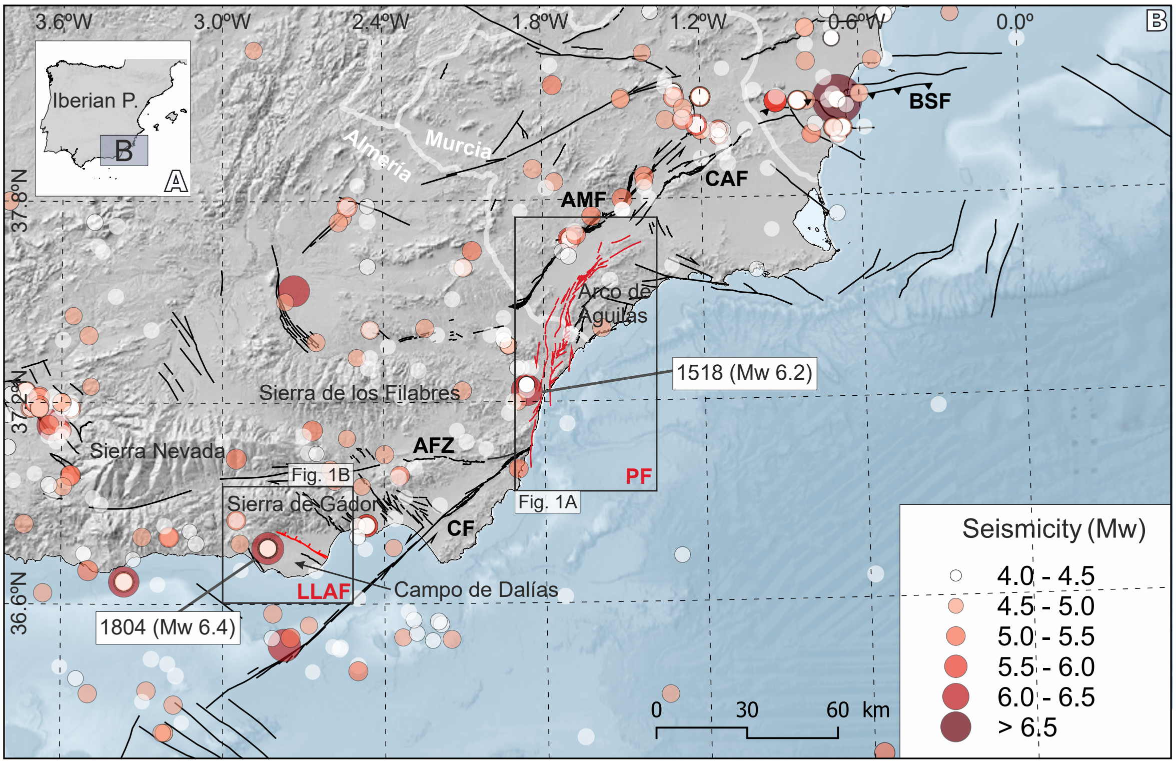

FIGURE 1. Seismotectonic setting of southeastern Iberia (location indicated in A inset) showing the main active faults from the QAFI database (García-Mayordomo *et al.*, 2012). The Palomares Fault (PF) and Llano del Águila Fault (LLAF) are highlighted in red. Seismicity from 1048 to 2011 is shown (Instituto Geográfico Nacional (IGN), 2012), highlighting historical earthquakes that caused significant damage provably associated with both faults. CF: Carboneras Fault, AFZ: Alpujarras Fault Zone, Fault, AMF: Alhama de Murcia Fault, CAF: Carrascoy Fault, BSF: Bajo Segura Fault.

25, 1804 Dalías earthquake (IEMS IX and estimated Mw ~6.4), the most significant event in a seismic sequence that strongly impacted the Campo de Dalías area, was likely generated by the LLAF, possibly in combination with the nearby Loma del Viento Fault (De Pro-Díaz *et al.*, 2023; Molins-Vigatà *et al.*, 2022; Murphy-Corella, 2019).

Palomares Fault

The PF is one of the major faults in the region in the EBSZ and forms the western boundary of the Arco de Águilas (Coppier *et al.*, 1989), an arc-shaped structure consisting of a succession of ridges and Neogene basins (Fig. 1). This structure reflects deformation associated with the indentation of a tectonic block that transfers compression from the eastern Algerian margin into the eastern Betics. (*e.g.* Coppier *et al.*, 1990; Palano *et al.*, 2015). The fault is predominantly a left lateral strike-slip fault with subvertical fault plane and horizontal slickenside lineations displaying pitches of up to 10º toward the south (Bousquet *et al.*, 1976; Coppier *et al.*, 1990; Weijermars, 1987). To date, only a few studies have focused on the PF geomorphological and structural expression (Booth-Rea *et al.*, 2004; Bousquet *et al.*, 1975; Roquero *et al.*, 2019; Silva *et al.*, 1993).

The fault zone is broad and complex, comprising multiple fault strands. Due to its predominantly lateral displacement (minor vertical offset), and distributed deformation, the surface expression of the fault is subtle compared to other faults within the system. These conditions do not produce prominent scarps, making them especially prone to erosion from alluvial processes and land use modifications. In recent decades, extensive agricultural development in the area has erased much of the original surface expression of the fault, which was still observable prior to these anthropic changes (Fig. 2).

Llano del Águila Fault

The LLAF is located in the Campo de Dalías (Fig. 1). It is a normal fault with dextral strike-slip component trending NW-SE, with an estimated surface length of ~20 km. This fault offsets Quaternary alluvial fans draining the Sierra de Gádor (Molins-Vigatà *et al.*, 2022), the dominant topographic relief in the area. The Campo de Dalías is characterized by a network of faults and rotated crustal blocks. These blocks are confined by the Carboneras Fault (CF) to the southeast and the Alpujarras Fault Zone system (AFZ) to the north (Fig. 1), that are part of a larger wedge-shaped structure, which may be undergoing westward

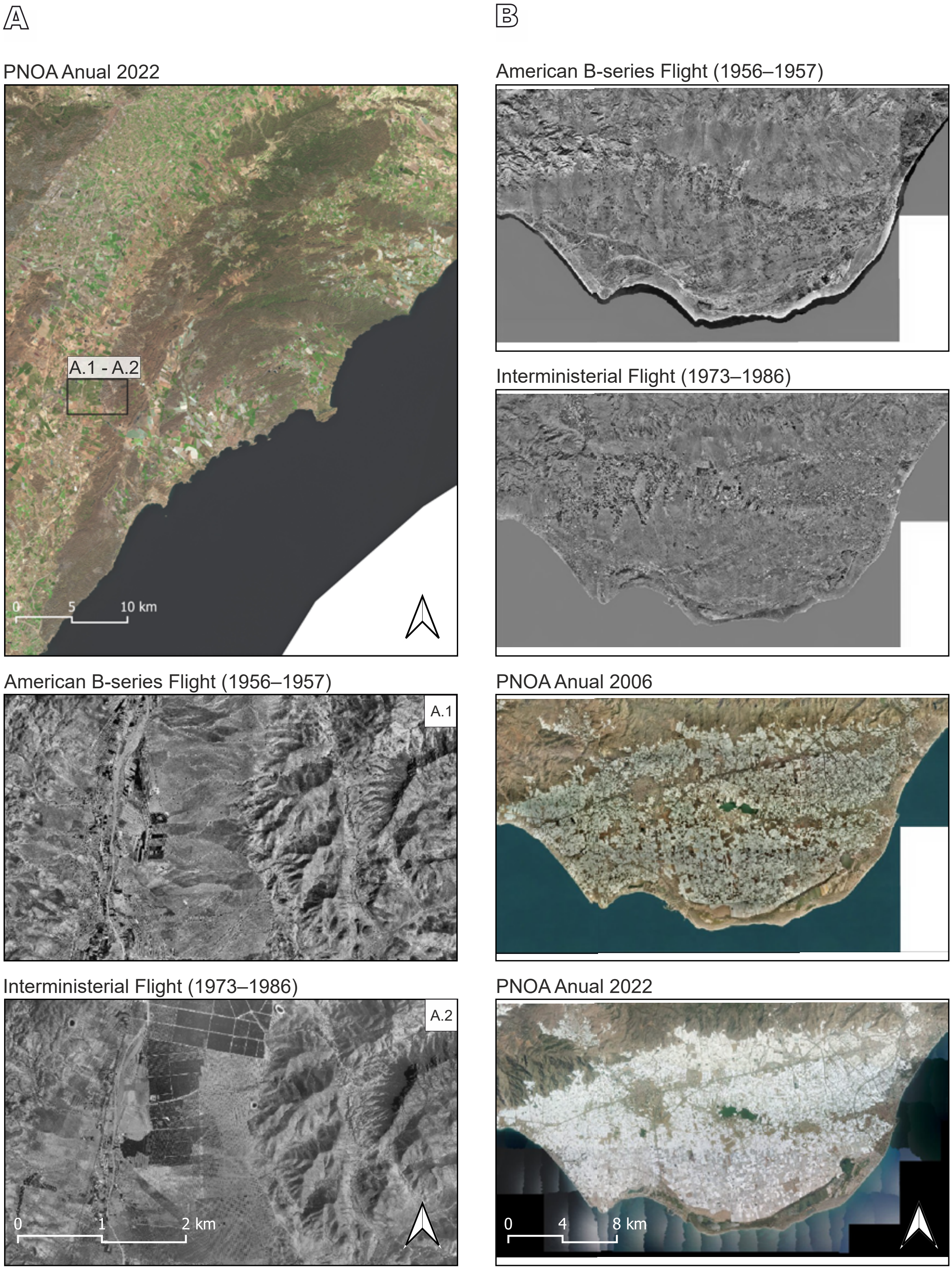

FIGURE 2. A) Palomares fault area, showing the current landscape and two detailed examples where the two images datasets used for the DSM reconstruction can be compared (A.1 and A.2; location indicated in A). It is clearly observed that, in the Interministerial flight imagery (1973-1986), the Palomares fault area already exhibits significant anthropogenic modifications. B) Temporal evolution of land cover in the Campo de Daías agricultural area. All orthophotos were obtained from the IGN web services (Centro Nacional de Información Geográfica, CNIG, 2025). Location indicated in Figure 2.

displacement (Martínez-Díaz and Hernández-Enrile, 2004). The LLAF is part of a set of extensional faults that share a similar orientation, including the Loma del Viento and the Balanegra faults (Galindo-Zaldívar *et al.*, 2003; Marín-Lechado *et al.*, 2005; Pedrera *et al.*, 2012).

The surface expression of the LLAF is more prominent compared to the PF due to its greater vertical displacement. As a normal fault, it is characterized at surface by decametric fault scarps that cut across multiple generations of alluvial fans in the area. However, the region has undergone extensive land modification due to intensive agricultural activity. Campo de Dalías serves as a clear example for the application of this methodology, as almost no natural topography remains unaltered, with nearly the entire area covered by greenhouses (Fig. 2).

DATA

Images

For the study area of the PF, two DSMs were generated: i) AmB-PF using images from the American B-series flight and ii) InM-PF using images from the Interministerial flight. For the LLAF area, only one DSM was produced, InM-LLAF, based on images from the InM flight (Table 1).

The AmB and the InM flights were the first historical aerial surveys to cover the entire Spanish territory with high image density, 60% forward and 30% side overlap (Centro Nacional de Información Geográfica, CNIG, 2025). However, the processing of these datasets poses challenges due to the low radiometric resolution (Pérez *et al.*, 2014) of the scanned images (8-bit), the absence of camera calibration data, variable preservation and scanning quality, all of which affect the accuracy and reliability of derived products. Moreover, since both datasets were acquired over extended periods and with multiple camera systems, image properties can vary within the same dataset, further complicating their use in consistent photogrammetric workflows.

The aerial images of the AmB flight were acquired by the United States Air Force in agreement with Spanish authorities between 1956 and 1957. Unlike the earlier American A-series flight (1945–1946), which had limited geographic scope and reconnaissance purposes, the B-series mission was designed for photogrammetric applications and provided systematic

TABLE 1. Image information summarized from the three different DSMs. Information from: Centro Nacional de Información Geográfica (CNIG, 2025)

DSM	Flight	Camera	Scale	Spatial Resolution	Focal length (mm)	Date	Num. images
AmB-PF	American Serie-B	XF361	1:32000	21 µm ~67 cm (GSD)	153.01	02/05/1956	13
						03/06/1956	7
		SF259			151.92	02/07/1956	7
		RF5641			154.19	03/08/1956	5
		SF269			151.42	25/02/1957	10
						15/03/1957	3
InM-PF	Interministerial	UAg 1078	1:18000	15 µm ~27 cm (GSD)	152.77	03/1979 05/1979	84
						07/1977	112
		UAg 1052			153.26	02/1977	28
		UAgI 6019			152.96	07/1977	18
		Uag 1056			152.24	07/1977	25
InM-LLAF	Interministerial	UAg 1056	1:18000	25 µm ~45 cm (GSD)	152.24	07/1979	46
		UAg 1098			151.52	09/1977	1

coverage of the entire national territory (Pérez *et al.*, 2014). The InM flight represents the first complete photogrammetric survey conducted by the Spanish administration between 1973 and 1986. It was followed by successive campaigns that ultimately led to the current National Plan for Aerial Orthophotography (PNOA), managed by the Instituto Geográfico Nacional (IGN). The AmB flight images are held by the Cartographic Centre of the Spanish Air Force (CECAF) and can be purchased on demand, whereas the InM flight images are freely available from the IGN web services. All image and camera information are available from IGN web services (CNIG, 2025).

A total of 45 images were used to perform the AmB-PF model, which are from four different cameras and in different time sets (Table 1). The images from the XF361, SF259 and RF5641 cameras were taken during 1956, all in different month sets between May and August. The images from the remaining camera (SF269) were taken during January and February of 1957. The images have a scale of 1:32,000 with a Ground Sample Distance (GSD) of ~67 cm per pixel (CNIG, 2025).

A total of 267 images were used to perform the InM-PF. The images used from this flight are from four different cameras, most of them from February or August 1977 and the rest from May 1979 (Table 1). The scale of these images is 1:18,000, with GSD of ~27 cm per pixel (CNIG, 2025).

For InM-LLAF, a total of 47 images were used. These images were captured by the same camera, in July 1977 except for one, taken by the camera UAg 1098, acquired in September 1977 (Table 1). The scale for these images is 1:18,000. Although the images used for InM-LLAF belong to the same flight as those used for InM-PF, spatial resolution is lower, with GSD of ~45 cm per pixel (CNIG, 2025).

The images from the InM flight generally exhibit better specific features including scale, resolution and image acquisition timing (Table 1), as described above, suggesting that the resulting DSM is expected to be of higher quality compared to that of the AmB flight. Nonetheless, for the PF we generated a model using the AmB flight because these images capture significantly less anthropogenic terrain modification, given their prior acquisition (Fig. 1), and may provide valuable information that is not preserved in the InM flight. In the LLAF sector, only the InM flight was used to generate a DSM, as the early anthropogenic modifications present in this imagery apparently do not affect the fault scarps.

Ground Control Points (GCPs)

Ground Control Points (GCPs) were used to scale and georeference the DSMs. In this study, all GCPs are virtual (vGCP), meaning they were not physically marked or measured in the field, but were instead manually identified using available orthophotos for each study area (CNIG, 2025). The points were placed at unchanged, clearly recognizable locations visible in the AmB, InM and the current orthophoto (PNOA 2022, 0.25 m resolution), avoiding surfaces altered by human activity or natural processes, and ensuring a well-distributed spatial coverage (Tonkin and Midgley, 2016).

For AmB-PF, a total of 88 GCPs were used, for InM-PF a total of 91 GCPs and InM-LLAF 33 GCPs. The number of GCPs varies depending on the total coverage area; as a reference, approximately one GCP was used for every 6 to 10 km^2.

METHODS

Historical Aerial Image processing

The historical aerial photographs used for the generation of the three DSMs were all processed following the same workflow (Fig. 3).

Since these are analog images, not originally acquired in digital format, their digitization requires special care to ensure that they are suitable for photogrammetric analysis. In particular, the scanning process must preserve key geometric references, such as the fiducial marks, which define part of the internal geometry of the camera. Ideally, any deformation in scanned images should be corrected using fiducial marks and the fiducial coordinate system provided in the camera calibration certificates (Knuth *et al.*, 2023; Pérez *et al.*, 2014). However, several scanned image sets, used in this study, had cropped fiducial marks or notches in the camera field, and calibration certificates are not available. Despite these limitations, some partial information about the internal camera parameters, such as the focal length printed on the image margins, could still be retrieved. Although incomplete, this information was incorporated as input for the camera calibration process within the photogrammetric workflow, supporting the self-calibration procedures implemented in SfM photogrammetric software. To exclude the camera field and other features (*e.g.* sea, imperfections in the photogram) during the processing, individual masks were made for each image.

For the georeferentiation process Easting and Northing coordinates of the vGCPs were extracted using QGIS (QGIS Development Team, 2021) and height values were sampled from the available 2 × 2 m DEM (Instituto Geográfico Nacional, 2016). GCPs were placed using the available AmB and InM orthophotos

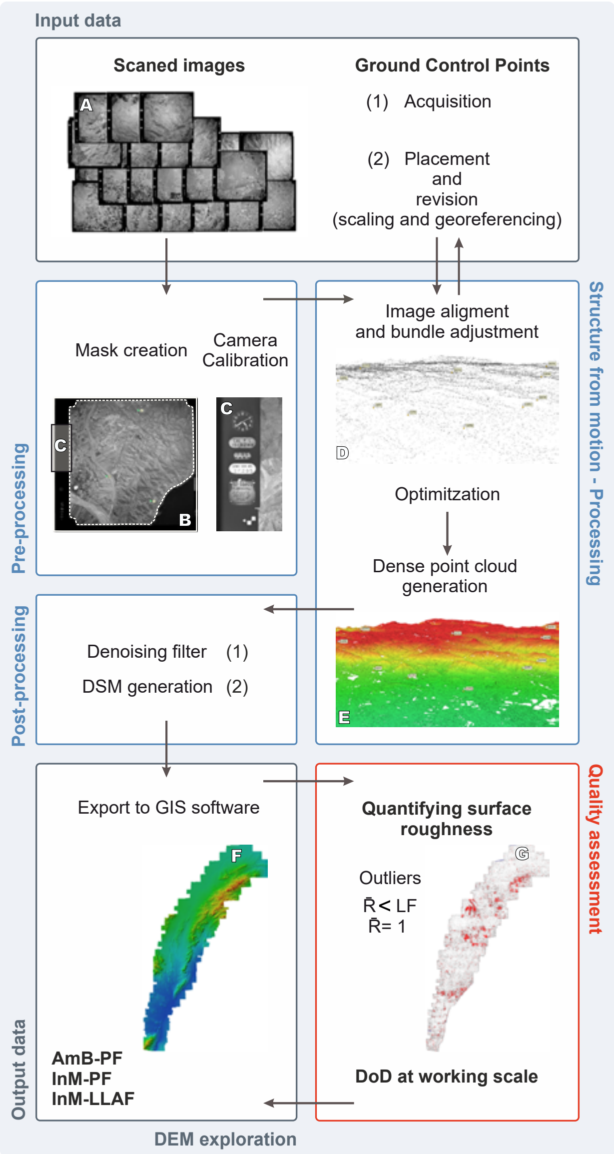

FIGURE 3. Workflow followed for each DSM reconstruction. A) Example of overlapping images used. B) Scanned photogram, white dotted line shows the mask done in photogram margins and coastline, to be excluded from processing. C) Camera information found on the image margin. D) Sparse point cloud with tie points found during image matching alignment. E) Dense point cloud. F) Final DSM generated. G) Example of spatial distribution of Surface Roughness.

of the area, according to the imagery used to generate each DSM. Since InM orthophotos are only available for the Almería region, and the PF area is partially located in Murcia (Fig. 1), all GCPs for InM-PF were referenced using the AmB orthophoto. This approach ensured internal consistency of the input data and avoided positional discrepancies between orthophotos from different flights.

All datasets were processed using Agisoft Metashape (vers. 2.0.1). Typical SfM-MVS workflow was followed (*e.g.* Eltner *et al.*, 2016; Snavely *et al.*, 2008): i) Image alignment, involving the identification of homologous points in overlapping images; ii) Bundle Adjustment (BA), in which both the external (extrinsic) orientation parameters and the internal (intrinsic) camera parameters are estimated; iii) Scaling and georeferencing of the model; iv) Optimization and v) Dense point cloud generation, reconstructing a high-density 3D point cloud from the aligned images.

During the BA, camera self-calibration was performed to estimate intrinsic parameters such as focal length, principal point, and lens distortion. Internal camera parameters, as previously described, were incorporated into this step, along with vGCPs used for georeferencing. Including GCPs during BA significantly reduces error propagation and improves the accuracy of the self-calibration process (Eltner *et al.*, 2016). When necessary, this step was repeated to correct errors related to vGCPs placement, followed by reprocessing of the image alignment and BA. Following BA, optimization of the camera parameters was conducted to minimize reprojection errors and improve the spatial accuracy of the tie points.

Subsequently, dense point clouds and depth maps were generated, providing the basis for the final DSM products. Prior to DSM generation, a noise reduction filter was applied to the dense point clouds using CloudCompare (Cloud Compare Development Team, 2021), effectively removing outliers and improving the quality of the data. The DSMs were then produced from these filtered point clouds. During this process, extrapolation was enabled to fill gaps in areas lacking sufficient image overlap or matching points, thereby ensuring continuous surface models.

The DSM spatial resolution was fixed at 2 m, which was selected as the working scale, resulting in approximately 1.5 to 3 points per pixel. Using a finer resolution was discarded, as it introduced excessive noise in the models. In this case, these are DSMs, as they include surface features such as buildings and vegetation.

The main indicators of DSM quality used were the Root Mean Square Error (RMSE) from GCPs and the reprojection error. The RMSE calculated from GCPs, provides a general measure of the georeferencing accuracy by quantifying the average difference between the known GCP positions and their estimated positions in the model. The reprojection error, on the other hand, reflects how accurately the software was able to align the original image points with the reconstructed 3D geometry during BA. It is expressed in pixels, and values close to or below 0.5 are generally considered indicative of a good internal model fit.

Quantifying Surface Roughness

There are multiple approaches to quantify Surface Roughness (Smith, 2014), in this case, we estimated local variability in slope and aspect across the DSMs (Hobson, 1972; McKean and Roering, 2004; Sappington *et al.*, 2007). Unlike other methods which primarily rely on slope or elevation differences, this approach also incorporates aspect to more fully characterize surface complexity (Sappington *et al.*, 2007), providing a finer and detailed estimation of Surface Roughness.

To estimate Surface Roughness, unit vectors normal to the surface are constructed for each DSM pixel, (equation 1). The coordinates from the unit vectors (x_i, y_i and z_i) (equation 2), are derived from the slope and aspect of each pixel, which correspond to the colatitude (φ_i) and longitude (φ_i) of the unit vector respectively.

$$R_i = \sqrt{(x_i^2+y_i^2+z_i^2)} \quad (1)$$

$$x_i = \sin\theta_i \cdot \cos\phi_i \qquad y_i = \sin\theta_i \cdot \sin\phi_i \qquad z_i = \cos\theta_i \quad (2)$$

The spatial distribution of these vectors within a given sampling window provides a measure of terrain Roughness. Mean Roughness ($\bar{R}$) is computed using a moving sampling window, where $\bar{R}$= 1 indicates smooth surface (Fig. 4A), characterized by highly similar unit vectors with in the same sampling window. Values lower than 1 reflect increasing Roughness (Fig. 4B), where unit vectors present greater dispersion. $\bar{R}$ was calculated on the DSMs at 5 pixel (10 m) sampling window. This window size captures fine-scale variations and allows the detection of $\bar{R}$ anomalies introduced during DSM generation. The results were visualized as Roughness raster layers for each DSM.

Outlier values were identified in each DSM classified as maximum and Minimum Roughness outlier, with the goal of detecting instrumental artifacts. By establishing threshold values for outliers, it is possible to determine which areas of the DSMs are less reliable and should be treated with caution during interpretation (Fig. 4B). For statistical outlier detection only, and to reduce data volume and computational cost, each Roughness raster was subsampled to a resolution of 100 m. Once the thresholds were defined, outliers were identified in the original 2 × 2 m Roughness rasters.

Maximum Roughness outliers, which corresponds to highly irregular surfaces, are represented by low numerical $\bar{R}$ values. On natural terrains, $\bar{R}$ values are typically expected to follow a right-skewed distribution, with most values clustering around $\bar{R} \approx 0.98$ (Sappington *et al.*, 2007). To identify the most extreme Roughness (*i.e.* artifacts of instrumental or processing origin), we defined a threshold corresponding to the Low Fence (LF), calculated as 1.5 times the interquartile range below the first quartile. Values below this threshold were interpreted as non-natural Roughness and classified as Maximum Roughness outliers (Fig. 4C).

Minimum Roughness outliers were defined as areas with a $\bar{R}$ value of exactly 1, a value not expected on natural

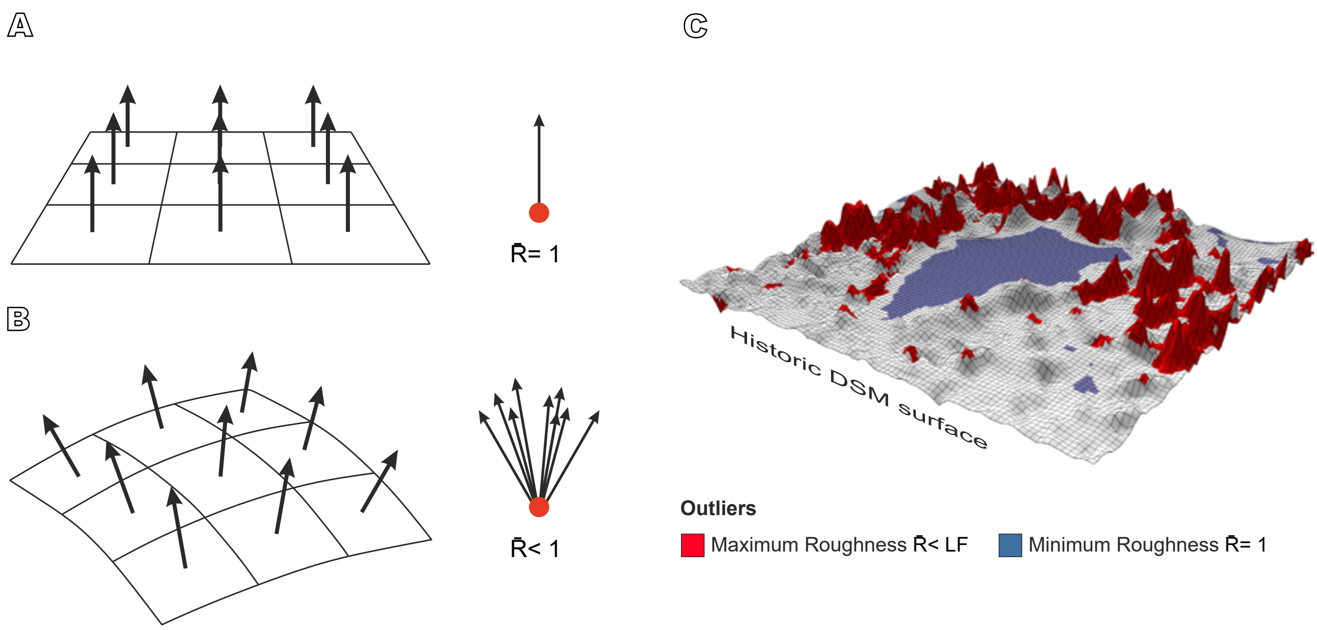

FIGURE 4. Schematic graphic representation of Surface Roughness calculation. A) Example of low Roughness. B) Example of high Roughness. C) Example of outlier detection. The defined outlier thresholds highlight surfaces with anomalous Roughness values that clearly do not correspond to natural terrain variability (LF: Low Fence).

surfaces, representing anomalously smooth surfaces. These regions reflect areas where image correlation failed. While extrapolation was enabled during DSM generation to fill data gaps, this additional filtering step was applied to exclude extrapolated surfaces larger than the sampling window (10 m), ensuring that only reliable interpolations were retained for further analysis (Fig. 4C).

DEM of difference (DoD) at a working scale

To support detailed morphometric interpretations at a finer (working) scale, DoD analyses were carried out to assess the vertical accuracy of the produced DSMs. As previously noted, precise spatial accuracy is not a strict requirement for this type of study, and therefore the DoD results may reflect residual georeferencing errors inherent to the DSMs.

DoDs were generated by subtracting each DSM from the current DEM, also used in the georeferencing process. During this computation, pixels corresponding to Roughness outliers were excluded, as these values do not correspond to actual topographic variations. This procedure was applied to three selected areas, one for each DSM, where fault traces are no longer visible due to anthropogenic modification. These areas were selected based on previous studies in the region and regional geological mapping.

To further validate the DSM accuracy, DoD values from anthropogenically altered areas were compared against those from stable, unmodified zones. These zones were selected through visual inspection of the DSMs, AmB and InM imagery, and current DEMs and orthophotos, independently of the DoD results. This comparison may also highlight elevation changes related to natural processes, such as channel erosion, landslides, or rockfalls. However, in the studied areas, fault traces mainly occur within basin floors, where the occurrence of such processes is limited, as they typically develop on hillslopes. Moreover, these processes are generally spatially localized and therefore easily identifiable and manageable, and are not expected to significantly influence the overall DoD signal.

RESULTS

DSMs properties

Key properties of the resulting models, automatically reported by the photogrammetric software after BA, are summarized in Table 2. In addition, we also describe the actual overlap between images (Fig. 5).

AmB-PF, covers a total area of 902 km² and was generated from 45 images. The RMSE based on GCPs was approximately 0.55 m, and the reprojection error 0.46 pixels indicating good overall performance of this DSM image overlap reaches up to six images covering the same area (Fig. 5).

TABLE 2. Principal DSM properties summarized

	AmB-PF	InM-PF	InM-LLAF
Num. images	45	267	47
Coverage area (km^2)	902	1110	210
GCPs RMSE (m)	0.55	3.65	2.72
Reproj. Error (px)	0.46	1.25	1.27

InM-PF is the largest of the three models, covering an area of 1110 km² and comprising 241 images. The RMSE was 3.65 m, and the reprojection error 1.25 pixels, both higher than those obtained for the AmB-PF. The InM flight images provide higher image overlap, with up to nine or more images covering the same area (Fig. 5).

InM-LLAF was the smallest model, covering 210 km² using a total of 47 images. The RMSE for GCPs was 2.72 m, and the reprojection error 1.27 pixels. These results were broadly comparable to those of InM-PF, as both were generated from the same flight dataset. Image overlap is similarly high, with up to nine or more images covering the same area (Fig. 5).

Roughness assessment

Overall, Surface Roughness values and patterns are comparable to those observed in modern DEMs, with most $\bar{R}$ values ranging between 0.98 to 1 (Fig. 6), except in problematic areas where Roughness outliers are present. These outliers are commonly organized in linear bands, reflecting systematic artifacts rather than isolated noise (Fig. 7). In addition, some DSMs display a baseline Roughness, unrelated to natural surface variability, detected under visual inspection and corresponding to artificial Roughness introduced during photogrammetric processing. $\bar{R}$ distribution and outlier values vary depending on the DSM, particularly influenced by the images used for their generation.

Around 12.19% of the AmB-PF area shows outliers: 5.38% were Maximum Roughness outliers and around 6.81%, Minimum Roughness outliers. Maximum Roughness was considered for $\bar{R}$< 0.945 (Figs. 6; 7). These values were generally scattered across the whole region with some significant continuous clusters (Fig. 7A). A significant presence of anomalously smooth surfaces ($\bar{R}$= 1 or Minimum outliers) was also detected. Beyond these

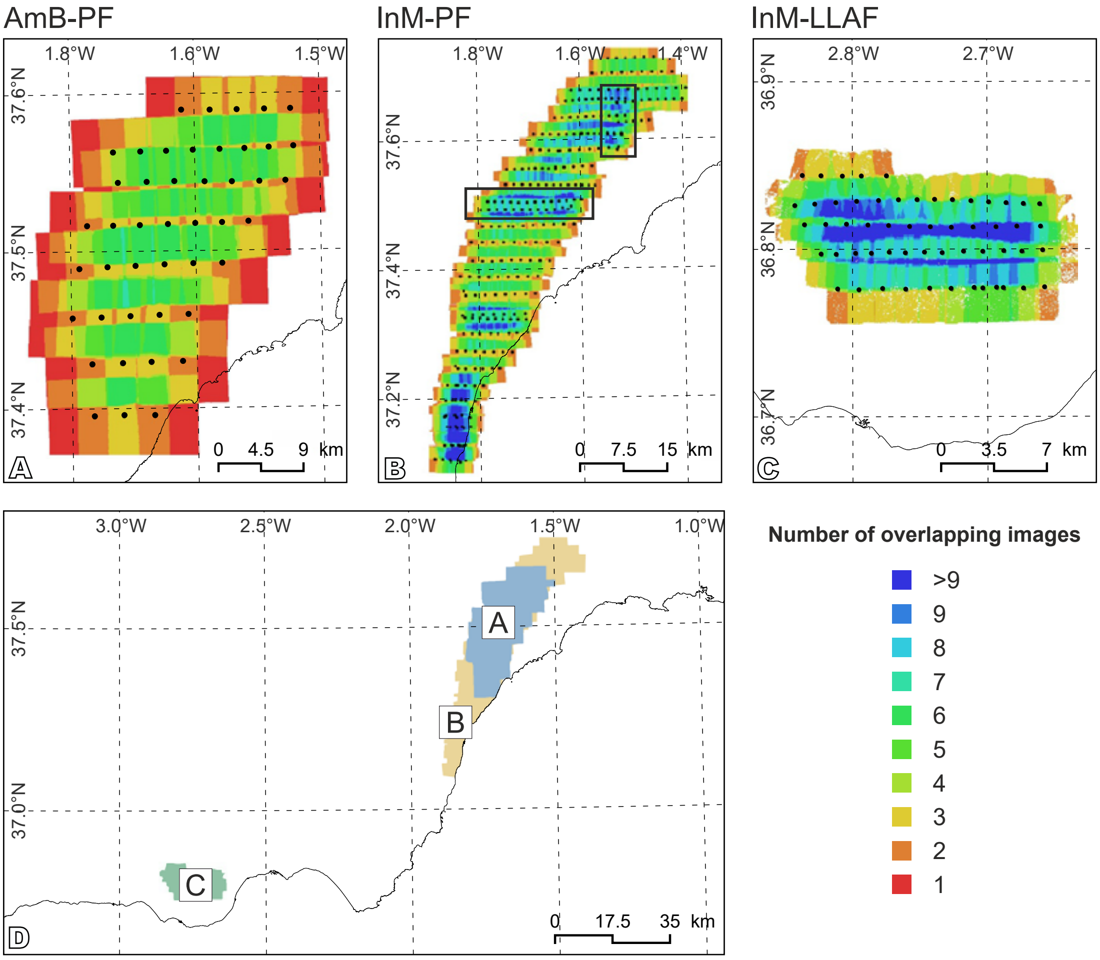

FIGURE 5. Image overlap for each DSM. Black dots indicate camera locations, estimated by the photogrammetric software. The black polygons in panel B highlights overlap between images acquired at different dates. In panel A, most overlaps involve images of different ages, whereas in panel C only one image was acquired at a different date. The locations of A, B and C are shown in panel D.

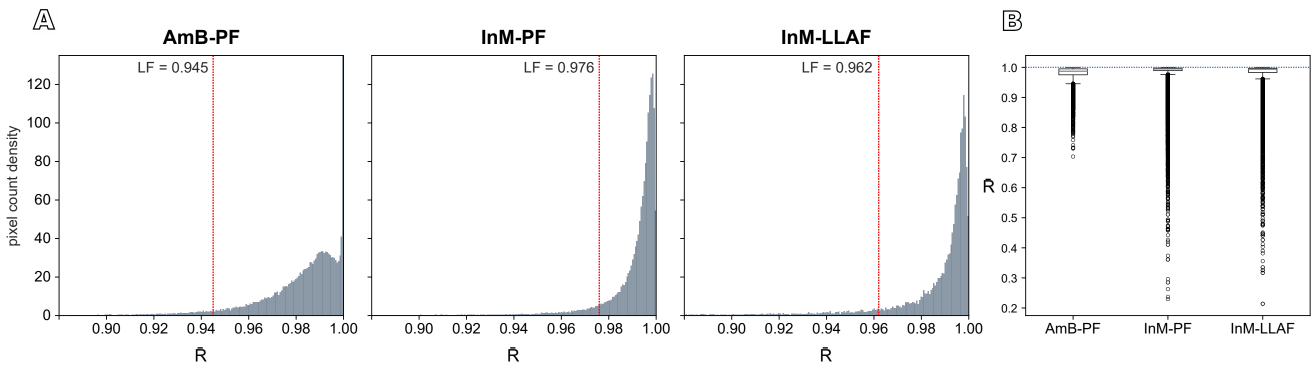

FIGURE 6. Maximum Roughness outlier detection. A) Density histograms of $\bar{R}$ values for each DSM. The red line indicates the LF threshold used to identify Maxim Roughness outliers ($\bar{R}$< LF). B) Boxplots of $\bar{R}$ values for each DSM, highlighting the distribution of Maximum Roughness outliers (black points), the blue line indicates Minimum Roughness outliers at $\bar{R}$= 1.

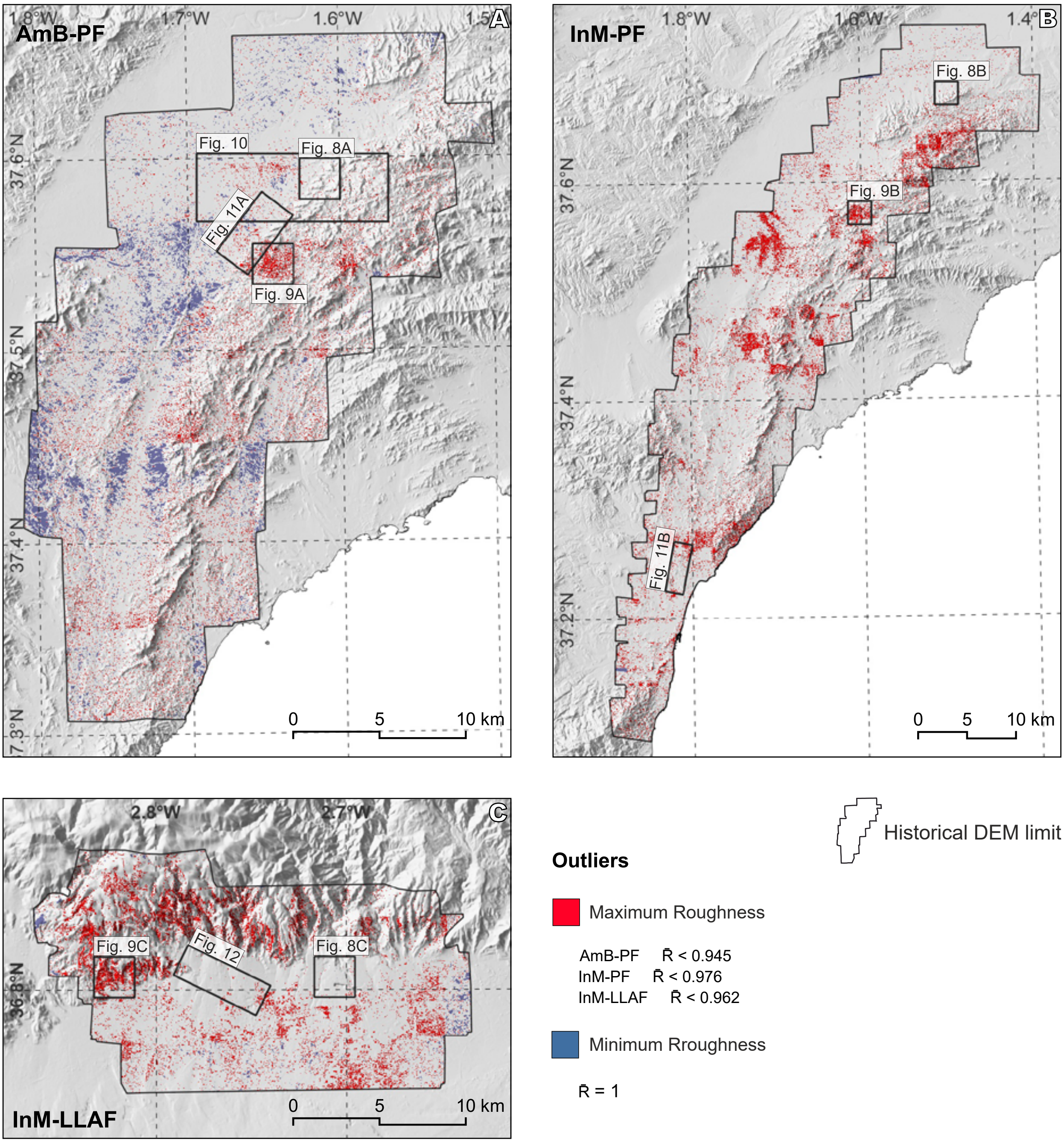

FIGURE 7. Spatial distribution of Surface Roughness outliers for each DSM. Maps showing all Surface Roughness values are provided in the supplementary material (Molins-Vigatà *et al.*, 2025).

statistically defined outliers, the AmB-PF DSM exhibits a pervasive fine-scale baseline Surface Roughness across the entire model. These values are not captured by the applied outlier thresholds but are interpreted as processing-related artefacts, based on their spatial pattern and systematic distribution. This baseline Roughness is characterized by a high frequency of $\bar{R}$ values between approximately 0.98 and 0.99, producing a broad and systematic shift in the $\bar{R}$ distribution (Fig. 6A). This pattern contrasts with the steeper and more compact $\bar{R}$ distributions observed in the InM-derived DSMs (Fig. 6).

InM-PF exhibited approximately 10.51% of outlier values (10.10% Maximum and 0.41% Minimum), while InM-LLAF showed around 13.40% (12.31% Maximum and 1.09 Minimum) (Figs. 6; 7). Maximum Roughness was considered for regions with $\bar{R}$ below 0.976 and 0.962 for the InM-PF and InM-LLAF models, respectively (Fig. 6B, C). In both cases, Maximum Roughness outliers were primarily concentrated in specific areas, forming large clusters (Fig. 7B, C), while Minimum Roughness, was scarce (Fig. 7B, C). For these DSMs baseline Roughness was considerably reduced or almost absent. This pattern was reflected in their Roughness distribution plots (Fig. 6B, C), which show strongly right-skewed distributions with lower dispersion compared to the AmB-PF.

ACCURACY AND QUALITY OF THE DSMS

DSMs placement accuracy

The three DSMs generated in this study exhibit placement accuracies within the expected range for models derived from historical aerial imagery. The reported errors are of the same order of magnitude as those documented in previous studies using these flight series. Mestre-Runge *et al.* (2023) generated a model using 42 images from the InM flight, achieving a reprojection error of 0.822 pixels and a mean absolute error of 1.12 m. Aguilar *et al.* (2013), also using the InM flight, reported GCP RMSE values of approximately 0.5 m from a dataset of eight images Studies based on AmB imagery, using 3 to 4 photos from a single strip, reported vertical errors ranging from 1 to 3 m (Pérez-Álvarez *et al.*, 2013), between 2.87 and 3.15 m (Picon-Cabrera *et al.*, 2020) and around 2 m (Aguilar *et al.*, 2013). In comparison, he InM-derived models produced in this study, show slightly higher errors (3.65 m and 2.72 m), whereas the AmB-PF shows considerably lower errors (0.55 m) than those reported in previous works. It is noteworthy that the models generated in this study are a significantly larger area and are based on a substantially greater number of photographs, which may influence the resulting error values.

The InM flight appears to offer more favorable characteristics for DSM generation as it features a larger flight scale, higher image resolution (Table 1), and greater image overlap (Fig. 5) compared to the AmB flight. However, the DSM derived from the AmB flight shows lower geolocation and reprojection errors than the two DSMs generated from InM imagery (Table 2). This differences in geolocation accuracy is counterintuitive, as generally, higher image resolution, greater overlap, and a well-distributed GCP network should improve the accuracy of the processed model (O'Connor *et al.*, 2017). However, in historical imagery the opposite trend is often observed (Bermúdez-González *et al.*, 2024). This behavior may be related to the absence of full camera calibration, in this situation, the software relies on blind self-calibration, and higher resolution can amplify local distortions (*e.g.* lens or film deformation), leading to higher errors. By contrast, lower-resolution imagery may act as a smoothing factor, attenuating small-scale distortions and resulting in lower reprojection and GCP errors.

It is also important to consider limitations in the GCP network. Although the spatial distribution of GCPs can be considered adequate, all control points used in this study are virtual GCPs (vGCPs), whose coordinates were extracted from existing datasets rather than measured directly in the field, introducing additional uncertainty. Moreover, although the total number of GCPs is comparable relative to the area covered, the ratio of GCPs per image differs significantly between flights due to differences in flight scale. In the InM models, the lower GCPs to image ratio means that the BA is more strongly constrained by tie points than by control points. In contrast, the higher GCP density in the AmB-PF model results in a more GCPs constrained block geometry, potentially leading to an over-constrained adjustment (Villanueva and Blanco, 2019) but yielding lower GCP RMSE values. It should be emphasized that RMSE reflects only the fit of the model to the reference GCPs and does not necessarily represent the overall geometric quality or internal consistency of the 3D reconstruction.

Roughness as a quality indicator

Polidori and Hage (2020) pointed out that most DEM artifacts primarily affect slope more than elevation and advocated for visual inspection as a key method for identifying such issues. In our case, we observe that such artifacts are also strongly associated with aspect, as they often manifest through abrupt changes in slope orientation. This highlights the particular effectiveness of Surface Roughness, estimated with unit vectors, for detecting subtle photogrammetric inconsistencies, since it incorporates both slope and aspect into the Roughness calculation.

Under visual inspection, all three models display areas of both well-resolved (Fig. 8) and poorly-resolved (Fig. 9) topography, directly correlated to the amount of Roughness outliers in the area. In well-resolved zones, Roughness outliers represent only ~2% of the surface, allowing for reliable interpretation of geomorphological features. By contrast, poorly-resolved zones Roughness outliers cover up to 30-40% depending on the DSM, thereby hindering accurate morphologic interpretation of any kind. The Roughness in Figure 8 and 9 corresponds only to outlier values. However, the AmB-PF model exhibits a generally higher baseline Roughness. While Maximum Roughness was detected and flagged, this widespread baseline Roughness remains present across the surface.

Arranged bands of Maximum Roughness are commonly found in overlapping areas between images (Fig. 7). These overlaps often involve photographs taken on different dates, and in some cases, even years apart, as well as with different cameras. It is therefore reasonable to expect that such heterogeneity in image acquisition conditions leads to increased Roughness in those regions. The AmB-PF was generated from imagery acquired with four different cameras over several years (Table 1), introducing greater variability in image quality and acquisition geometry, resulting in systematic bands of Roughness anomalies across most overlap zones (Fig. 7A), showing also high density of baseline Roughness. In contrast, the InM DSMs show less or even negligible baseline Roughness, with Maximum Roughness values appearing in localized clusters (Fig. 7B, C). In the InM-PF DSM, clusters of Maximum Roughness also coincide with overlaps between images acquired at different times but these overlaps are less frequent and localized (Figs. 5B; 7B). These are easier to detect and manage, which improves their usability. These differences are likely related to the higher image resolution, more uniform acquisition parameters and higher density of matched features, aided by better image contrast and overlap of the InM flight.

Clusters of Maximum Roughness outliers are also observed in mountainous areas with buildings, or other infrastructures (Fig. 7). These areas typically exhibit complex image textures, which are often poorly resolved in the photogrammetric processing (Eltner and Sofia, 2020). InM-PF and InM-LLAF present a higher proportion of Maximum Roughness outliers (10.10% and 12.31%, respectively) compared with 5.38% for AmB-PF. This difference is linked to the distinct distribution of $\bar{R}$ values in each DSM. The AmB-PF is noisier and shows a disperse distribution which results in a lower LF threshold (Fig. 6A). In contrast, the InM DSMs exhibit a steeper distribution concentrated toward higher Roughness values, yielding higher LF thresholds and therefore classifying more pixels as outliers (Fig. 6A). This configuration makes Maximum Roughness outlier detection in InM-PF and InM-LLAF more robust, as the $\bar{R}$ values interpreted as artifacts in these DSMs are clearly distinct from those of natural terrain surfaces, ranging from the LF to 0. In AmB-PF, by contrast, the Roughness values from natural terrain surface is mixed with baseline Roughness and the distribution shows a shorter tail (Fig. 6B), with outliers extending only from the LF to 0.614, complicating the separation between true geomorphic features and processing artifacts.

Minimum Roughness outliers are typically found in regions with low image contrast, such as agricultural fields, where the matching of common points is more challenging. In some cases, these outliers appear arranged in rectilinear bands, likely highlighting areas of poor image overlap and inconsistencies between cameras, similar to those observed for Maximum Roughness values. Combining extrapolation filtering during DSM generation with Roughness analysis improves quality control (Fig. 10). This approach allows for the selective retention of only the most reliable extrapolated areas. In the AmB-PF model, which exhibits the highest percentage of Minimum Roughness outliers, excluding extrapolated zones entirely would have resulted in significant data loss (Fig. 10). In contrast, the InM-PF and InM-LLAF models, with lower percentages of Minimum Roughness (Fig. 7B, C), exhibited fewer extrapolated areas, likely due to a higher density of matched features, aided by better image contrast and overlap.

Once outliers have been identified, the DSM pixels corresponding to these values can be removed to exclude them from any subsequent analyses for which the DSM is used, such as slope calculations, local relief analysis, topographic profiling, or simple visual inspection of the surface. Alternatively, these pixels may be retained, provided that their spatial distribution is known and that

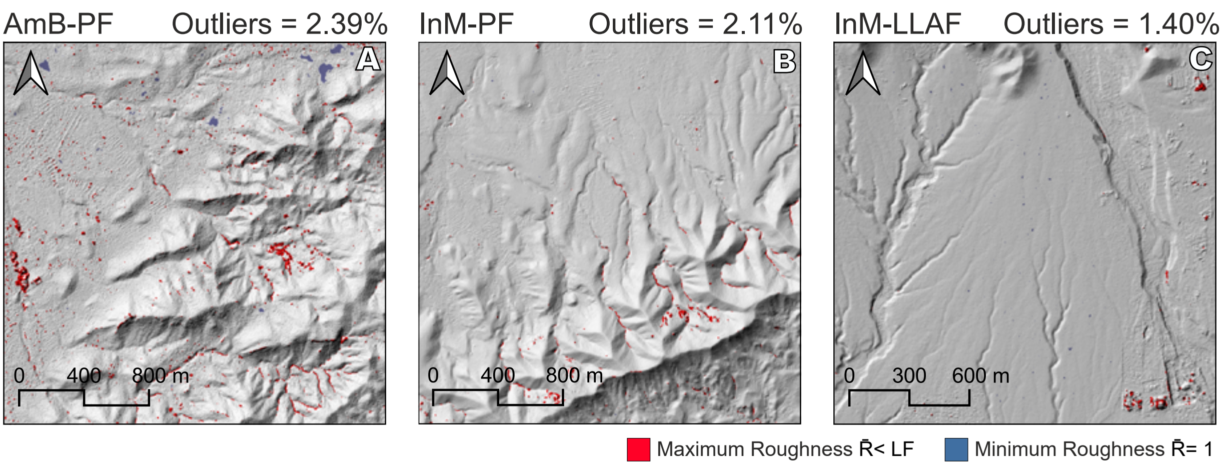

FIGURE 8. Examples of well-resolved areas for each DSM. The corresponding outlier values are displayed for each area in red and blue.

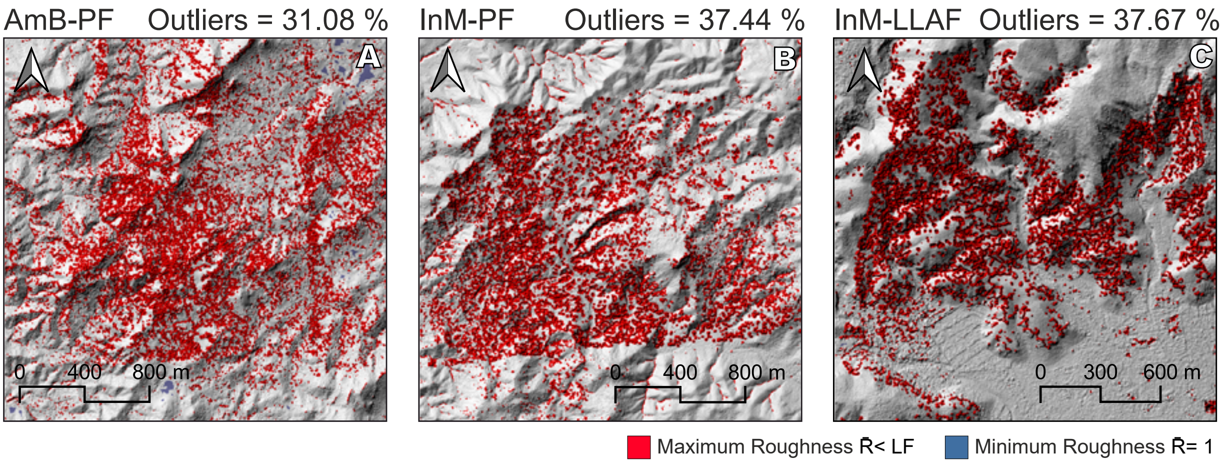

FIGURE 9. Examples of poorly-resolved areas for each DSM. The corresponding outlier values are displayed for each area in red and blue.

they are recognized as not representing valid natural surface conditions.

SUITABILITY OF DSMS FOR MORPHOTECTONIC STUDIES

Study cases

For each DSM, a zone was selected where anthropogenic modifications had erased the surface expression of the fault (Figs. 11; 12). In these selected areas, DSMs enabled the reconstruction and analysis of fault traces that are no longer preserved. Topographic profiles were generated, and a DoD analysis was carried out to evaluate DSM consistency, thereby determining their suitability for supporting detailed morphotectonic studies.

Palomares Fault

As an example of near-fault geomorphic expression using AmB-PF, a faint and partially degraded fault scarp was recognized at the northern termination of the fault (Fig. 11A), where the Lorca–Águilas highway now crosses the area. This feature represents a very gentle fault escarpment, with a NE–SW orientation and approximately 1 meter high. Its expression is very subtle, and it is nearly unrecognizable in the present-day DEM.

Another example using InM-PF is found in a fault strand, with a N–S orientation, located northwest of Palomares village (Fig. 11B), where the first outcrop of the PF was discovered, giving the fault its name (Bousquet and Phillip, 1976). This outcrop, along with its surface expression, has been completely erased by agricultural activity. Although no clear vertical offset is recognized, the scarp was previously

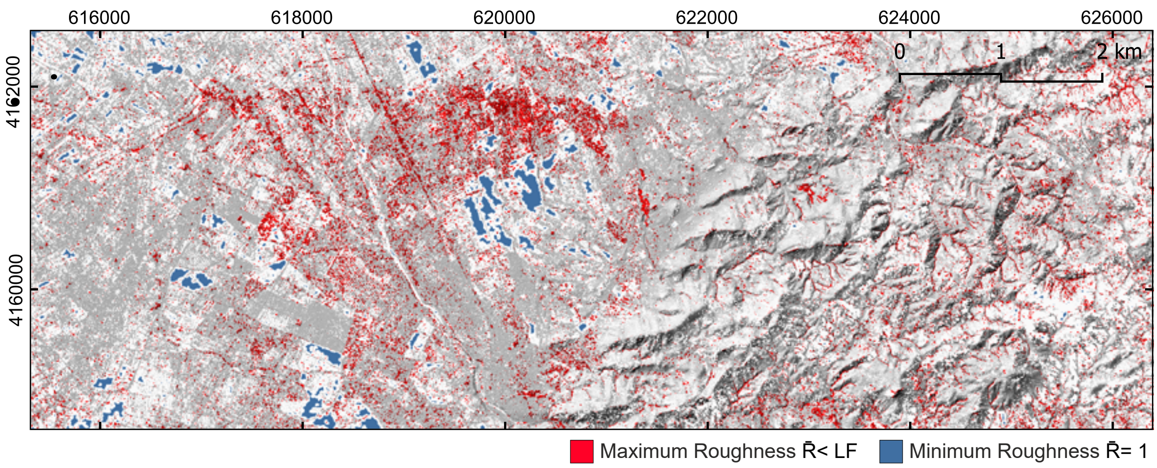

FIGURE 10. Non-extrapolated hillshade of the AmB-PF DSM. The white spots in the figure correspond to areas that were extrapolated in the final AmB-PF DSM. The Roughness assessment enables filtering of these zones, keeping only the most reliable extrapolated areas.

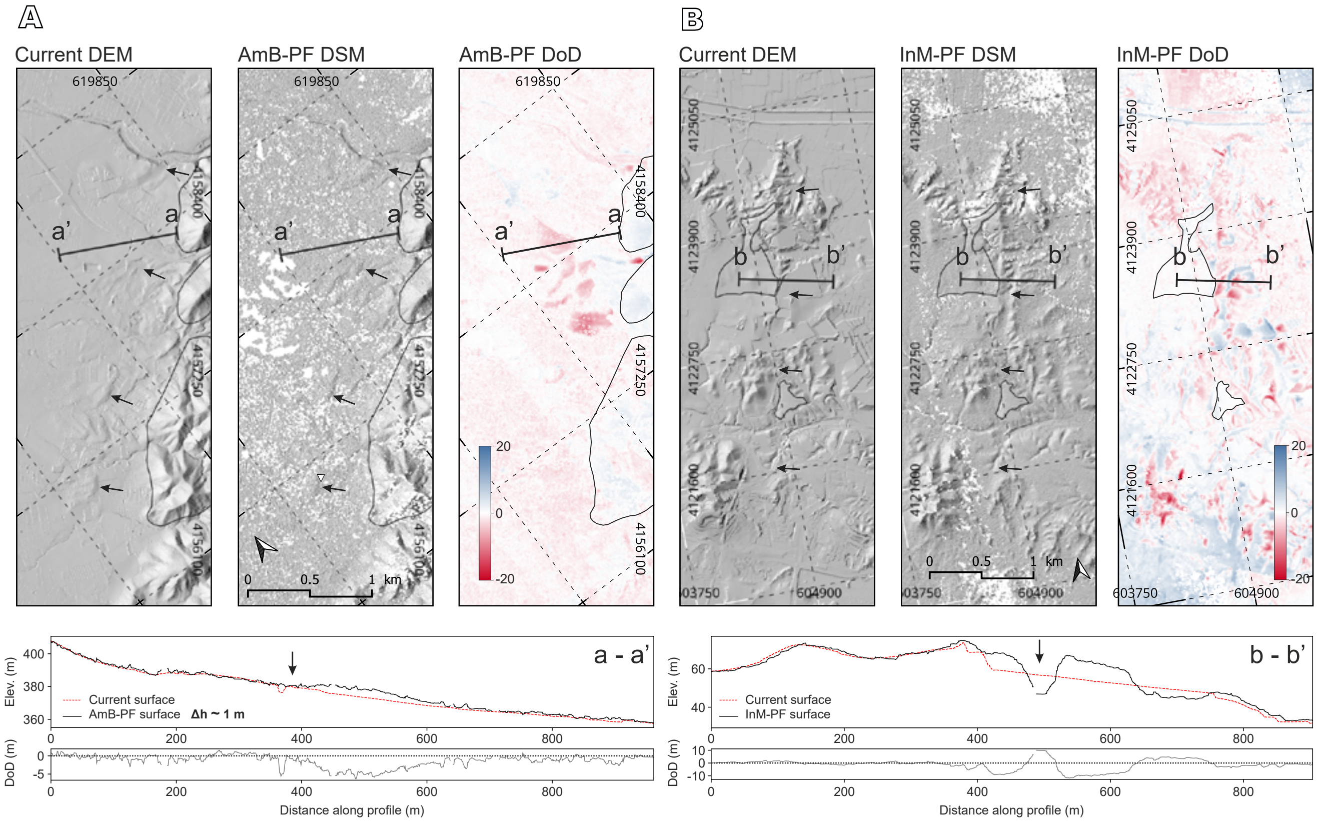

FIGURE 11. Examples where historical DSMs enable near-fault detailed morphotectonic analysis for A) AmB-PF and B) InM-PF. DSMs are shown after, excluding pixels corresponding to Roughness outlier values. All three map sets share the same scale, indicated on the corresponding DSM. Black outlined polygons indicate unmodified areas over time, black profile lines indicate the position of the topographic profiles below and black arrows indicate the location of the fault traces. The plotted profiles allow comparison between the surfaces derived from the historical DSMs and the current DEM, while DoD profile plots show the elevation differences between the two models.

clearly recognizable, in the InM images, due to drainage incision, around 20 m deep, that followed the fault trace. This feature is revealed in topographic profiles extracted from the DSM, which capture the former expression of the fault at surface, now absent in the current DEM.

Llano del Águila Fault

In the LLAF region some fault scarp segments remain recognizable, thanks to their more pronounced geomorphic expression, but it is currently impossible to perform detailed morphometric analyses departing from present day topography (Fig. 12), such as estimating cumulative vertical offset or completing a comprehensive fault mapping. This is the case for the two decametric fault scarps that run in the campo de Dalías, completely covered by greenhouses (Fig. 1B). In the DSM, these fault strands are clearly recognizable not only because of the prominent scarps, but also due to the ongoing erosional processes affecting the beheaded uplifted surface, which is disconnected from the active fluvial drainage system. Topographic profiles across these scarps using the historical DSMs also reveal how the original morphology has been completely altered (Fig. 12).

The apparent vertical displacement estimated from the different topographic profiles illustrates how anthropogenic modifications currently hinder accurate fault scarp characterization. In the a-a' profile (Fig. 12), no vertical displacement is observed using the current DEM, whereas the DSM reveals a clear scarp approximately ~3 m high. In the b-b' profile, a subtle scarp is perceptible in the current topography, but its height cannot be reliably estimated. However, the DSM allows the estimation of an apparent offset of ~3 m. In the c-c' profile, the current DEM permits only a very uncertain estimation due to surface modification caused by an excavation located directly on the fault scarp, which has altered its original morphology. In contrast, the DSM enables a more reliable assessment, revealing a scarp height of ~6 m. These comparisons demonstrate that offsets derived from the present-day DEM, in this case, systematically can underestimate the true scarp height, highlighting the value of DSMs for accurate morphotectonic analysis.

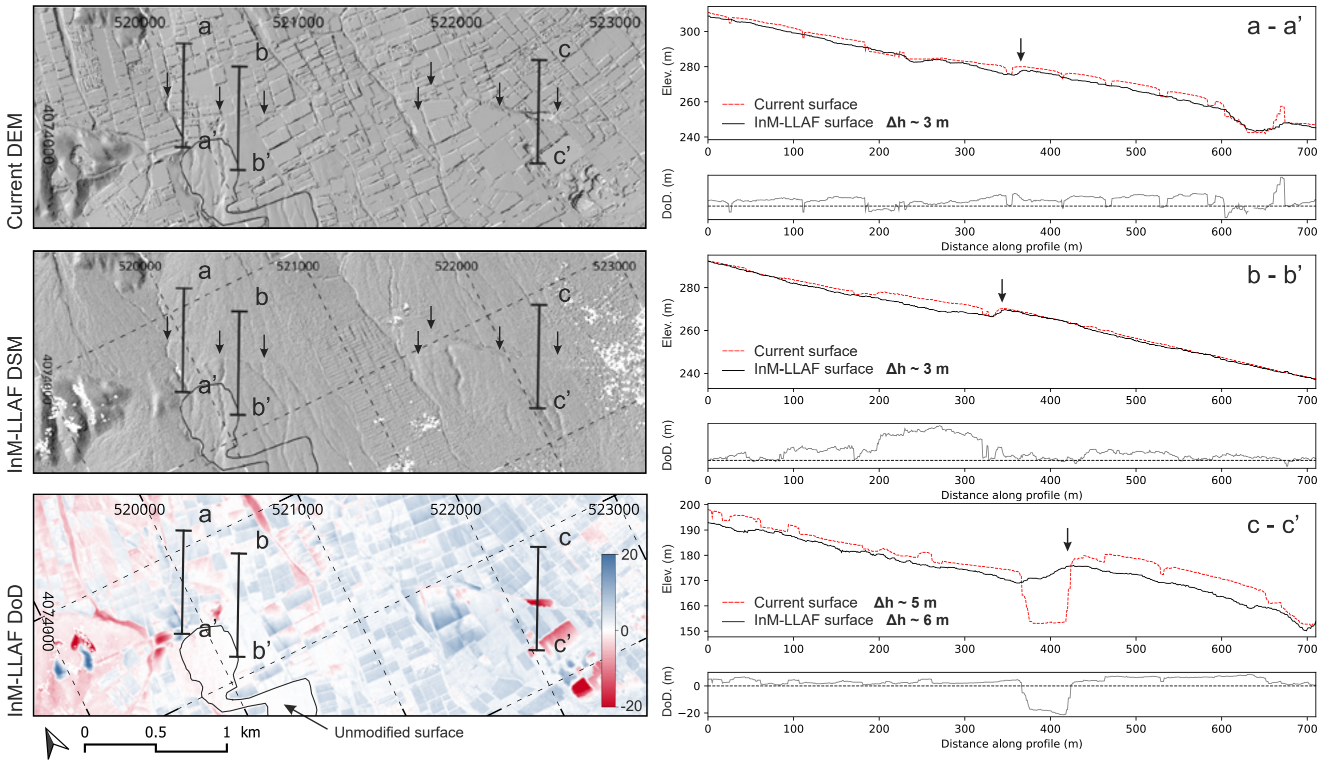

FIGURE 12. Examples where historical DSMs enable near-fault detailed morphotectonic analysis for InM-LLAF. DSM is shown after, excluding pixels corresponding to Roughness outlier values. All three maps share the same scale. Black outlined polygons indicate surfaces that remained unmodified over time, black profile lines the position of the topographic profiles shown on the right and black arrows indicate the location of the fault. The plotted profiles allow comparison between the surfaces derived from the historical DSMs and the current DEM, while the DoD profile plots show the elevation differences between the two models.

DoD analyses

The DoD maps, across the selected study areas, primarily reveal anthropogenic changes in land use. In each case, specific zones where the surface has remained unaltered over time were identified and marked within the detailed study areas (Figs. 11A, B; 12). In both InM-PF and InM-LLAF, the DoD maps show that elevation changes in unmodified areas are close to zero. In contrast, AmB-PF exhibits noticeable elevation differences even in zones that have not undergone surface modification (Fig. 11A). The analysis of DoD density histograms, together with the comparison of DoD values for the entire area versus the unmodified areas, provides a clear assessment of the performance and reliability of the DSMs (Fig. 13).

For InM-PF and InM-LLAF, elevation changes in unmodified areas are centered around zero with low dispersion, indicating both the preservation of the original topographic signal and consistency of the DSMs. For InM-PF (Fig. 13B), the mean elevation difference across the entire area is –0.22 m (SD= 2.66 m), whereas in unmodified zones the mean shifts to 0.20 m with a substantially lower standard deviation (SD= 0.92 m). In the case of InM-LLAF (Fig. 13C), the mean elevation difference for the whole area is 1.76 m (SD= 3.22 m), reflecting the high degree of anthropogenic modification in this region; in unmodified areas, the mean decreases to –0.03 m with a markedly reduced dispersion (SD= 0.53 m). These characteristics confirm their suitability for detailed morphotectonic investigations.

The AmB-PF DSM exhibits a mean elevation difference of approximately –0.67 m (SD= 1.49 m) across the entire area, and 0.38 m (SD= 1.49 m) for the stable zones. The mean of the unmodified zones is slightly lower than that of the entire area, while the standard deviation remains identical. Elevation differences are still observed in the anthropogenically unmodified zones and are also detectable in the DoD maps (Fig. 11A). The origin of these differences cannot be attributed to human activity or other active processes, such as ongoing erosion. Their presence is likely related to the baseline Roughness detected across the entire DSM, leading to this “noise” appearance in both the AmB-PF DSM and the DoD map, which is not observed in the InM derived products. While the AmB-PF DSM is suitable for identifying and mapping active faults or for

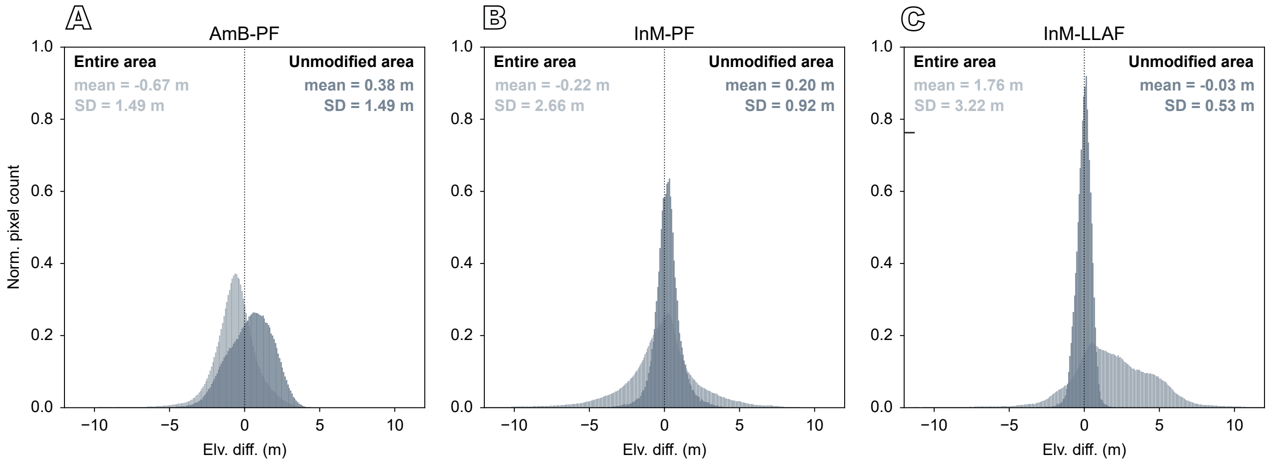

FIGURE 13. DoD density histogram comparison between the entire area of each selected study zone (light gray) and the corresponding unmodified areas (dark gray), shown in Figure 11 and 12. Results from A) AmB-PF, B) InM-PF and C) InM-LLAF.

general morphotectonic analyses, it is less appropriate for detailed quantitative studies.

CONCLUSIONS

By implementing an accessible workflow and incorporating Surface Roughness as a quality-assessment metric, we were able to generate extensive and reliable high-resolution DSMs (2 m resolution) with low positional error (0.55, 3.61 and 2.72 m). This methodology addresses a key limitation of previous studies using historical aerial imagery, which mainly focused on geolocation accuracy without assessing the quality of the reconstructed surface. Our approach enables the spatial evaluation of surface quality and the identification of potential artifacts or distortions, a critical requirement for geomorphological and morphotectonic studies that rely heavily on DEM quality. Performing DoD evaluations in each study area allows for assessing suitability of DSMs to support more advanced analyses. In this context, historical DSMs prove valuable not only for fault trace mapping but also for detailed quantitative geomorphological analysis.

All three DSMs exhibit both well- and poorly-resolved topographic areas. Well-resolved zones allow for reliable geomorphological mapping and, in the case of the InM DSMs, also enable more detailed studies, such as estimating vertical offsets for slip-rate calculations or assessing the spatial distribution of scarp displacements along fault systems. In contrast, the AmB-PF DSM is suitable for basic active fault mapping but less appropriate for detailed quantitative analyses, as reflected in the DoD results, due to its higher baseline Roughness.

Given that both datasets exhibit specific limitations and varying performance, the choice between these datasets should always consider their respective constraints and be tailored to the geomorphic and anthropogenic characteristics of the area under investigation, as well as to the specific objectives of the analysis. Notably, this methodology can be applied and reproduced with other analog aerial historical images under similar circumstances.

Overall, these results open new opportunities for morphotectonic investigations in regions where anthropogenic activity has obscured surface fault expressions, as well as for broader geomorphological studies involving landscape features that are no longer preserved in the present-day terrain.

ACKNOWLEDGMENTS

We would like to thank José J. Martínez-Díaz, Stephane Baize, and Matthieu Ferry for their contributions to the first phase of this research.

This research has the financial support of Project NSOURCES, grant PID2020-119772RB-I00 funded by MCIN/AEI/10.13039/501100011033. It was conducted in the frame of the predoctoral grant of Júlia Molins-Vigatà (PRE2021-097203) funded by MICIU/AEI/10.13039/501100011033.

SUPPLEMENTARY MATERIAL

The generated point clouds and DSMs, together with the GCP locations and coordinates and the Surface Roughness datasets, are available in an online repository under the CC-BY 4.0 license (Molins-Vigatà *et al.*, 2025).

REFERENCES

1956-1957 American Flight (B series), n.d. [Data set]. Centro Nacional de Información Geográfica (CNIG). Last accessed: September 2025. Website: https://centrodedescargas.cnig.es/CentroDescargas/home

1973-1986 Interministerial Flight, n.d. [Data set]. Centro Nacional de Información Geográfica (CNIG). Last accessed: September 2025. Website: https://centrodedescargas.cnig.es/CentroDescargas/home

Aguilar, M.A., Aguilar, F.J., Fernández, I., Mills, J.P., 2013. Accuracy Assessment of Commercial Self-Calibrating Bundle Adjustment Routines Applied to Archival Aerial Photography. The Photogrammetric Record, 28, 96-114. DOI: https://doi.org/10.1111/j.1477-9730.2012.00704.x

Bermúdez-González, J.L., Fernández Tapia, E., Castaño Perea, E., 2024. New Technologies in the Processing of European Digital Heritage and Their Application to the Historical Images of the American Flight of 1944 Over Spain. Future Cities and Environment, 10, 15, 1-15. DOI: https://doi.org/10.5334/fce.252

Blanch, X., Eltner, A., Guinau, M., Abellan, A., 2021. Multi-epoch and multi-imagery (Memi) photogrammetric workflow for enhanced change detection using time-lapse cameras. Remote Sensing, 13, 1460, 1-23. DOI: https://doi.org/10.3390/rs13081460

Blanch, X., Guinau, M., Eltner, A., Abellan, A., 2024. A cost-effective image-based system for 3D geomorphic monitoring: An application to rockfalls. Geomorphology, 449, 1-12. DOI: https://doi.org/10.1016/j.geomorph.2024.109065

Booth-Rea, G., Azanón, J.M., Azor, A., García-Duenas, V., 2004. Influence of strike-slip fault segmentation on drainage evolution and topography. A case study: The Palomares Fault Zone (southeastern Betics, Spain). Journal of Structural Geology, 26, 1615-1632. DOI: https://doi.org/10.1016/j.jsg.2004.01.007

Bousquet, J.-C., 1979. Quaternary Strike-slip Faults in Southeastern Spain. Tectonophysics, 52, 277-286. DOI: https://doi.org/10.1016/0040-1951(79)90232-4

Bousquet, J.C., Phillip, H., 1976. Observations microtectoniques sur la compression nord-sud quaternaire des Cordillères bétiques orientales (Espagne méridionales - Arc de Gibraltar). Bulletin de La Societé Géologique de France, 7, 711-724. DOI: https://doi.org/https://doi.org/10.2113/gssgfbull.S7-XVIII.3.711

Bousquet, J.C., Dumas, B., Montenat, C., 1975. Le décrochement de Palomarès: décrochement quaternaire senestre du bassin de Vera (Cordillères bétiques orientales, Espagne). Cuadernos de Geología, 6, 149-158.

Bramham, E.K., Wright, T.J., Paton, D.A., Hodgson, D.M., 2021. A new model for the growth of normal faults developed above pre-existing structures. Geology, 49, 587-591. DOI: https://doi.org/10.1130/G48290.1

Buforn, E., Udías, A., Mezcua, J., 1988. Seismicity and focal mechanisms in south Spain. Bulletin of the Seismological Society of America, 78, 2008-2024. DOI: https://doi.org/10.1785/BSSA0780062008

Bull, W.B., 2008. Tectonic geomorphology of mountains: A new approach to paleoseismology. Malden, Blackwell Publishing, 326pp.

Burbank, D.W., Anderson, R.S., 2013. Tectonic Geomorphology, Second Edition. Environmental & Engineering Geoscience, 19, 198-200. DOI: https://doi.org/10.2113/gseegeosci.19.2.198

CloudCompare Development Team, 2021. CloudCompare (version 2.12) [GPL software].

CNIG, 2025. Centro Nacional de Información Geográfica (CNIG), Centro de Descargas [WWW Document]. Last accessed: September 2025. Website: https://centrodedescargas.cnig.es/CentroDescargas/home

Coppier, G., Griveaud, P., De Larouziere, F.D., Montenat, C., Ott d'estevou, P., 1989. Example of Neogene tectonic indentation in the Eastern Betic Cordilleras: the Arc of Aguilas (Southeastern Spain). Geodinamica Acta, 3, 37-51. DOI: https://doi.org/10.1080/09853111.1989.11105173

Coppier, G., Ott D'Estevou, P., Montenat, C., 1990. Kinematics and paleogeographic evolution of the eastern Almeria basins. Documents et Travaux de l'Institut Géologique Albert de Lapparent, 12-13, 189-193.

De Pro-Díaz, Y., Perea, H., Insua-Arévalo, J.M., Martínez-Díaz, J.J., Canora, C., 2023. Constraining earthquake fault sources through the use of intensity data and seismic scenarios: application to the Betic Cordillera (South Spain). Frontiers in Earth Science, 11, 1214836, 1-20. DOI: https://doi.org/10.3389/feart.2023.1214836

Dietrich, J.T., 2016. Riverscape mapping with helicopter-based Structure-from-Motion photogrammetry. Geomorphology, 252, 144-157. DOI: https://doi.org/10.1016/j.geomorph.2015.05.008

Echeverria, A., Khazaradze, G., Asensio, E., Gárate, J., Dávila, J.M., Suriñach, E., 2013. Crustal deformation in eastern Betics from CuaTeNeo GPS network. Tectonophysics, 608, 600-612. DOI: https://doi.org/10.1016/j.tecto.2013.08.020

Elez, J., Silva, P.G., Pérez-López, R., Giner-Robles, J.L., Rodríguez-Pascua, M.A., Sánchez-Sánchez, Y., 2025. Estimating the potential consequences of historical Spanish earthquakes today: PAGER risk scenarios for seismic emergency management in Spain. Natural Hazards, 121, 11489-11521. DOI: https://doi.org/10.1007/s11069-025-07250-y

Eltner, A., Sofia, G., 2020. Structure from motion photogrammetric technique. In: Tarolli, P., Mudd, S.M. (eds). Developments in Earth Surface Processes: Remote Sensing of Geomorphology. Elsevier B.V., 23, 1-24. DOI: https://doi.org/10.1016/B978-0-444-64177-9.00001-1

Eltner, A., Kaiser, A., Castillo, C., Rock, G., Neugirg, F., Abellán, A., 2016. Image-based surface reconstruction in geomorphometry-merits, limits and developments. Earth Surface Dynamics, 4, 359-389. DOI: https://doi.org/10.5194/esurf-4-359-2016

Field, E.H., Working Group on California Earthquake Probabilities, 2015. UCERF3: A new earthquake forecast for California's complex fault system. U.S. Geological Survey Fact Sheet, 2015-3009, 6pp. DOI: https://doi.org/10.3133/fs20153009.

Galindo-Zaldívar, J., Gil, A.J., Borque, M.J., González-Lodeiro, F., Jabaloy, A., Marın-Lechado, C., Ruano, P., De Galdeano, C.S., 2003. Active faulting in the internal zones of the central Betic Cordilleras (SE, Spain). Journal of Geodynamics, 36, 239-250. DOI: https://doi.org/https://doi.org/10.1016/S0264-3707(03)00049-8

García-Mayordomo, J., Gaspar-Escribano, J.M., Benito, B., 2007. Seismic hazard assessment of the Province of Murcia (SE Spain): analysis of source contribution to hazard. Journal of Seismology, 11, 453-471. DOI: https://doi.org/10.1007/s10950-007-9064-0

García-Mayordomo, J., Insua-Arévalo, J.M., Martínez-Díaz, J.J., Jiménez-Díaz, A., Martín-Banda, R., Martín-Alfageme, S., Álvarez-Gómez, J.A., Rodríguez-Peces, M., Pérez-López, R., Rodríguez-Pascua, M.A., Masana, E., Perea, H., Martín-González, F., Giner-Robles, J., Nemser, E.S., Cabral, J., 2012. The Quaternary Active Faults Database of Iberia (QAFI v.2.0). Journal of Iberian Geology, 38, 285-302. DOI: https://doi.org/10.5209/rev_JIGE.2012.v38.n1.39219

García-Ruiz, J.M., 2010. The effects of land uses on soil erosion in Spain: A review. Catena, 81, 1-11. DOI: https://doi.org/10.1016/j.catena.2010.01.001

Gómez-Novell, O., García-Mayordomo, J., Ortuño, M., Masana, E., Chartier, T., 2020. Fault System-Based Probabilistic Seismic Hazard Assessment of a Moderate Seismicity Region: The Eastern Betics Shear Zone (SE Spain). Frontiers in Earth Science, 8, 1-25. DOI: https://doi.org/10.3389/feart.2020.579398

Gómez-Novell, O., Ortuño, M., García-Mayordomo, J., Insua-Arévalo, J.M., Rockwell, T.K., Baize, S., Martínez-Díaz, J.J., Pallàs, R., Masana, E., 2022. Improved Geological Slip Rate Estimations in the Complex Alhama de Murcia Fault Zone (SE Iberia) and Its Implications for Fault Behavior. Tectonics, 41, e2022TC007465, 1-30. DOI: https://doi.org/10.1029/2022TC007465

Herrero-Barbero, P., Álvarez-Gómez, J.A., Williams, C., Villamor, P., Insua-Arévalo, J.M., Alonso-Henar, J., Martínez-Díaz, J.J., 2021. Physics-Based Earthquake Simulations in Slow-Moving Faults: A Case Study From the Eastern Betic Shear Zone (SE Iberian Peninsula). Journal of Geophysical Research: Solid Earth, 126, e2020JB021133, 1-25. DOI: https://doi.org/10.1029/2020JB021133

Hobson, R.D., 1972. Surface Roughness in topography: quantitative approach. In: Chorley, R.J. (ed.). Spatial Analysis in Geomorphology. London, Methuen & Co., 221-245.

Instituto Geográfico Nacional (IGN), 2012. Catálogo de terremotos. Last accessed: September 2025. DOI: https://doi.org/10.7419/162.03.2022

Instituto Geográfico Nacional, 2016. Modelo Digital del Terreno 2x2 m (MDT02) [WWW Document], Centro de Descargas CNIG. Last accessed: September 2025. Website: https://centrodedescargas.cnig.es

Ioli, F., Dematteis, N., Giordan, D., Nex, F., Pinto, L., 2024. Deep Learning Low-cost Photogrammetry for 4D Short-term Glacier Dynamics Monitoring. PFG – Journal of Photogrammetry, Remote Sensing and Geoinformation Science, 92, 657-678. DOI: https://doi.org/10.1007/s41064-023-00272-w

James, M.R., Robson, S., 2012. Straightforward reconstruction of 3D surfaces and topography with a camera: Accuracy and geoscience application. Journal of Geophysical Research: Earth Surface, 117, 1-17. DOI: https://doi.org/10.1029/2011JF002289

Knuth, F., Shean, D., Bhushan, S., Schwat, E., Alexandrov, O., McNeil, C., Dehecq, A., Florentine, C., O'Neel, S., 2023. Historical Structure from Motion (HSfM): Automated processing of historical aerial photographs for long-term topographic change analysis. Remote Sensing of Environment, 285, 1-19. DOI: https://doi.org/10.1016/j.rse.2022.113379

Llena, M., Cavalli, M., Vericat, D., Crema, S., 2018. Assessing landscape changes associated to anthropic disturbances by means of the application of Structure from Motion photogrammetry using historical aerial imagery. Rendiconti Online Societa Geologica Italiana, 46, 74-81. DOI: https://doi.org/10.3301/ROL.2018.55

Lu, L., Zhou, Y., Walker, R.T., 2021. Using historical aerial photographs to measure earthquake deformation: Testing the effects of scan resolution. Remote Sensing of Environment, 252, 1-12. DOI: https://doi.org/10.1016/j.rse.2020.112118

Manighetti, I., Mercier, A., De Barros, L., 2021. Fault Trace Corrugation and Segmentation as a Measure of Fault Structural Maturity. Geophysical Research Letters, 48, 1-11. DOI: https://doi.org/10.1029/2021GL095372

Marín-Lechado, C., Galindo-Zaldívar, J., Rodríguez-Fernández, L.R., Serrano, I., Pedrera, A., 2005. Active faults, seismicity and stresses in an internal boundary of a tectonic arc (Campo de Dalías and Níjar, southeastern Betic Cordilleras , Spain). Tectonophysics, 396, 81-96. DOI: https://doi.org/10.1016/j.tecto.2004.11.001

Martín-Banda, R., Insua-Arévalo, J.M., García-Mayordomo, J., 2021. Slip Rate Variation During the Last ~210 ka on a Slow Fault in a Transpressive Regime: The Carrascoy Fault (Eastern Betic Shear Zone, SE Spain). Frontiers in Earth Science, 8, 1-21. DOI: https://doi.org/10.3389/feart.2020.599608

Martínez-Díaz, J.J., Hernández-Enrile, J.L., 2004. Neotectonics and morphotectonics of the southern Almería region (Betic Cordillera-Spain) kinematic implications. International Journal of Earth Sciences, 93, 189-206. DOI: https://doi.org/10.1007/s00531-003-0379-y

Martínez-Díaz, J.J., Masana, E., Ortuño, M., 2012. Tectónica activa de la falla de Alhama de murcia, Cordillera Bética, España. Journal of Iberian Geology, 38, 269-286. DOI: https://doi.org/10.5209/rev_JIGE.2012.v38.n1.39218

Martínez-Solares, J.M., Mezcua, J., 2002. Catálogo sísmico de la Península Ibérica:(880 a. C-1900). Dirección General del Instituto Geográfico Nacional, Monografía núm. 18, 256pp.

McCalpin, J.P., 2009. Chapter 3 Paleoseismology in Extensional Tectonic Environments. In: McCalpin, J.P. (ed.). Paleoseismology. International Geophysics, 95, 171-269. DOI: https://doi.org/10.1016/S0074-6142(09)95003-3

McCalpin, J.P., Ferrario, F., Figueiredo, P., Livio, F., Grützner, C., Pisarska-Jamroży, M., Quigley, M., Reicherter, K., Rockwell, T., Štěpančíková, P., Tábořík, 2023. New developments in onshore paleoseismic methods, and their impact on Quaternary tectonic studies. Quaternary International, 664, 59-76. DOI: https://doi.org/10.1016/j.quaint.2023.03.008

McKean, J., Roering, J., 2004. Objective landslide detection and surface morphology mapping using high-resolution airborne laser altimetry. Geomorphology, 57, 331-351. DOI: https://doi.org/10.1016/S0169-555X(03)00164-8

Mendoza-Fernández, A.J., Peña-Fernández, A., Molina, L., Aguilera, P.A., 2021. The Role of Technology in Greenhouse Agriculture: Towards a Sustainable Intensification in Campo de Dalías (Almería, Spain). Agronomy, 11, 101, 1-14. DOI: https://doi.org/10.3390/agronomy11010101

Mestre-Runge, C., Lorenzo-Lacruz, J., Ortega-Mclear, A., Garcia, C., 2023. An Optimized Workflow for Digital Surface Model Series Generation Based on Historical Aerial Images: Testing and Quality Assessment in the Beach-Dune System of Sa Ràpita-Es Trenc (Mallorca, Spain). Remote Sensing, 15, 1-24. DOI: https://doi.org/10.3390/rs15082044

Molins-Vigatà, J., García-Mayordomo, J., Ortuño, M., García-Sellés, D., Gómez-Novell, O., 2022. Caracterización geológica de la falla del Llano del Águila en Campo Dalías (Almería): posible fuente sismogénica del terremoto de 1804. Revista de la Sociedad Geológica de España, 35, 71-83. DOI: https://doi.org/10.55407/rsge.94908

Molins-Vigatà, J., Blanch, X., Martín-Banda, R., García-Mayordomo, J., Ortuño, M., García-Sellés, D., Gómez-Novell, O., García-Mayordomo, J., Martín-Banda, R., García-Sellés, D., Insua-Arévalo, J.M., Ortuño, M., 2025. Historical Digital Surface Models and Surface Roughness Maps from the Palomares and Llano del Águila Faults (Eastern Betics) [Data set], Zenodo. DOI: https://doi.org/https://doi.org/10.5281/zenodo.17236170

Moreno, X., 2010. Neotectonic and Paleoseismic onshore-offshore integrated study of the Carboneras Fault (Eastern Betics, SE Iberia). Barcelona, Universitat de Barcelona, 364pp.

Murphy-Corella, P., 2019. Los terremotos de Almería de 1804, En el archivo histórico nacional. Madrid, Instituto Geográfico Nacional, 600pp.

O'Connor, J., Smith, M.J., James, M.R., 2017. Cameras and settings for aerial surveys in the geosciences. Progress in Physical Geography: Earth and Environment, 41, 325-344. DOI: https://doi.org/10.1177/0309133317703092

Ortuño, M., Masana, E., García-Meléndez, E., Martínez-Díaz, J., Štěpančíková, P., Cunha, P.P., Sohbati, R., Canora, C., Buylaert, J.P., Murray, A.S., 2012. An exceptionally long paleoseismic record of a slow-moving fault: The Alhama de Murcia fault (Eastern Betic shear zone, Spain). Geological Society of America (GSA) Bulletin, 124, 1474-1494. DOI: https://doi.org/10.1130/B30558.1

Palano, M., González, P.J., Fernández, J., 2015. The Diffuse Plate boundary of Nubia and Iberia in the Western Mediterranean: Crustal deformation evidence for viscous coupling and fragmented lithosphere. Earth and Planetary Science Letters, 430, 439-447. DOI: https://doi.org/10.1016/j.epsl.2015.08.040

Pedrera, A., Marín-Lechado, C., Stich, D., Ruiz-constán, A., Galindo-Zaldívar, J., Rey-Moral, C., Lis, F., 2012. Nucleation, linkage and active propagation of a segmented Quaternary normal-dextral fault: the Loma del Viento fault (Campo de Dalías, Eastern Betic Cordillera, SE Spain). Tectonophysics, 522-523, 208-217. DOI: https://doi.org/10.1016/j.tecto.2011.12.001

Picon-Cabrera, I., Garcia-Gago, J.M., Sanchez-Aparicio, L.J., Rodriguez-Gonzalvez, P., Gonzalez-Aguilera, D., 2020. On the use of historical flights for the urban growth analysis of cities through time: The case study of avila (Spain). Sustainability, 12, 1-17. DOI: https://doi.org/10.3390/su12114673

Polidori, L., Hage, M. El, 2020. Digital elevation model quality assessment methods: A critical review. Remote Sensing, 12, 1-36. DOI: https://doi.org/10.3390/rs12213522

Portela, J., Staller, A., Béjar-Pizarro, M., Martínez-Díaz, J.J., Álvarez-Gómez, J.A., Khazaradze, G., 2025. New Insights on the Crustal Deformation in the Eastern Betics From Densified GNSS Data. Tectonics, 44, 1-24. DOI: https://doi.org/10.1029/2024TC008381

Pérez-Álvarez, J.A., Herrera, V.M., Martínez del Pozo, J., Ángel de Tena, M.T., 2013. Multi-temporal archaeological analyses of alluvial landscapes using the photogrammetric restitution of historical flights: A case study of Medellin (Badajoz, Spain). Journal of Archaeological Science, 40, 349-364. DOI: https://doi.org/10.1016/j.jas.2012.08.025

Pérez, J.A., Bascon, F.M., Charro, M.C., 2014. Photogrammetric Usage of 1956–57 Usaf Aerial Photography of Spain. The Photogrammetric Record, 29, 108-124. DOI: https://doi.org/10.1111/phor.12048

Purinton, B., Mueting, A., Bookhagen, B., 2023. Image Texture as Quality Indicator for Optical DEM Generation: Geomorphic Applications in the Arid Central Andes. Remote Sensing, 15(1), 85. DOI: https://doi.org/10.3390/rs15010085

QGIS Development Team, 2021. QGIS Geographic Information System.

Reitman, N.G., Bennett, S.E.K., Gold, R.D., Briggs, R.W., DuRoss, C.B., 2015. High-resolution trench photomosaics from image-based modeling: Workflow and error analysis. Bulletin of the Seismological Society of America, 105, 2354-2366. DOI: https://doi.org/10.1785/0120150041

Roquero, E., Silva, P.G., Rodríguez-Pascua, M.A., Bardají, T., Elez, J., Carrasco-García, P., Giner-Robles, J.L., 2019. Analysis of faulted fan surfaces and paleosols in the Palomares Fault Zone (Betic Cordillera, SE Spain): Paleoclimatic and paleoseismic implications. Geomorphology, 342, 88-102. DOI: https://doi.org/10.1016/j.geomorph.2019.06.003

Sappington, J.M., Longshore, K.M., Thompson, D.B., 2007. Quantifying Landscape Ruggedness for Animal Habitat Analysis: A Case Study Using Bighorn Sheep in the Mojave Desert. The Journal of Wildlife Management, 71, 1419-1426. DOI: https://doi.org/10.2193/2005-723

Silva, P.G., Goy, J.L., Somoza, L., Zazo, C., Bardají, T., 1993. Landscape response to strike-slip faulting linked to collisional settings: Quaternary tectonics and basin formation in the Eastern Betics, southeastern Spain. Tectonophysics, 224, 289-303.

Smith, M.W., 2014. Roughness in the Earth Sciences. Earth-Science Reviews, 136, 202-225. DOI: https://doi.org/10.1016/j.earscirev.2014.05.016

Snavely, N., Seitz, S.M., Szeliski, R., 2008. Modeling the world from Internet photo collections. International Journal of Computer Vision, 80, 189-210. DOI: https://doi.org/10.1007/s11263-007-0107-3

Stirling, M., McVerry, G., Gerstenberger, M., Litchfield, N., Van Dissen, R., Berryman, K., Barnes, P., Wallace, L., Villamor, P., Langridge, R., Lamarche, G., Nodder, S., Reyners, M., Bradley, B., Rhoades, D., Smith, W., Nicol, A., Pettinga, J., Clark, K., Jacobs, K., 2012. National Seismic Hazard Model for New Zealand: 2010 Update. Bulletin of the Seismological Society of America, 102, 1514-1542. DOI: https://doi.org/10.1785/0120110170

Stumpf, A., Malet, J.-P., Kerle, N., Niethammer, U., Rothmund, S., 2013. Image-based mapping of surface fissures for the investigation of landslide dynamics. Geomorphology, 186, 12-27. DOI: https://doi.org/10.1016/j.geomorph.2012.12.010

Taylor, L.S., Quincey, D.J., Smith, M.W., 2023. Evaluation of low-cost Raspberry Pi sensors for structure-from-motion reconstructions of glacier calving fronts. Natural Hazards and Earth System Sciences, 23, 329-341. DOI: https://doi.org/10.5194/nhess-23-329-2023

Tonkin, T., Midgley, N., 2016. Ground-Control Networks for Image Based Surface Reconstruction: An Investigation of Optimum Survey Designs Using UAV Derived Imagery and Structure-from-Motion Photogrammetry. Remote Sensing, 8(9), 786, 1-8. DOI: https://doi.org/10.3390/rs8090786

Valentini, A., Visini, F., Pace, B., 2017. Integrating faults and past earthquakes into a probabilistic seismic hazard model for peninsular Italy. Natural Hazards and Earth System Sciences, 17, 2017-2039. DOI: https://doi.org/10.5194/nhess-17-2017-2017

Villanueva, J.K.S., Blanco, A.C., 2019. Optimization of Ground Control Point (GCP) configuration for Unmanned Aerial vehicle (UAV) survey using Structure From Motion (SFM). The International Archives of the Photogrammetry, Remote Sensing and Spatial Information Sciences, XLII-4/W12, 167-174. DOI: https://doi.org/10.5194/isprs-archives-XLII-4-W12-167-2019

Weijermars, R., 1987. The Palomares brittle-ductile Shear Zone of southern Spain. Journal of Structural Geology, 9, 130-157.

Westoby, M.J., Brasington, J., Glasser, N.F., Hambrey, M.J., Reynolds, J.M., 2012. 'Structure-from-Motion' photogrammetry: A low-cost, effective tool for geoscience applications. Geomorphology, 179, 300-314. DOI: https://doi.org/https://doi.org/10.1016/j.geomorph.2012.08.021

Wheaton, J.M., Brasington, J., Darby, S.E., Sear, D.A., 2010. Accounting for uncertainty in DEMs from repeat topographic surveys: improved sediment budgets. Earth Surface Processes and Landforms, 35, 136-156. DOI: https://doi.org/10.1002/esp.1886

Woessner, J., Laurentiu, D., Giardini, D., Crowley, H., Cotton, F., Grünthal, G., Valensise, G., Arvidsson, R., Basili, R., Demircioglu, M.B., Hiemer, S., Meletti, C., Musson, R.W., Rovida, A.N., Sesetyan, K., Stucchi, M., 2015. The 2013 European Seismic Hazard Model: key components and results. Bulletin of Earthquake Engineering, 13, 3553-3596. DOI: https://doi.org/10.1007/s10518-015-9795-1

Yazdi, P., García-Mayordomo, J., Álvarez-Gómez, J.A., Gaspar-Escribano, J.M., Masana, E., 2023. Exploring the Connection of XVI-Century Major Historical Earthquakes in the Eastern Betic Cordillera, Spain: Insights From Viscoelastic Relaxation of the Lithosphere. Tectonics, 42, e2023TC007917, 1-17. DOI: https://doi.org/10.1029/2023TC007917

Yazdi, P., García-Mayordomo, J., 2024. Active Fault Interaction in the Eastern Betic Cordillera: A Model of Coseismic and Postseismic Stress Transfer Following Historical Earthquakes in SE Spain. Tectonics, 43, e2024TC008383, 1-21. DOI: https://doi.org/10.1029/2024TC008383

Manuscript received October 2025;
revision accepted March 2026;
published March 2026.

Models digitals de superfície derivats d'imatges aèries històriques en àrees altament antropitzades aplicats a l'estudi de falles actives (Bètiques orientals, Espanya)

Resum

El reconeixement de les formes del relleu i l'anàlisi de la superfície terrestre són elements clau en els estudis geomorfològics i morfotectònics. En particular, l'estudi detallat de l'expressió superficial de les falles actives és essencial per caracteritzar-les com a generadores de sismicitat dins dels models d'avaluació de perillositat sísmica. Tanmateix, l'augment de l'activitat antropogènica ha alterat profundament el paisatge natural, degradant o esborrant les formes tectòniques i limitant la caracterització acurada de les falles actives en moltes regions del món. Un exemple paradigmàtic és el sud-est de la Península Ibèrica, on l'intens desenvolupament agrícola de les darreres dècades ha transformat completament el paisatge natural. Per afrontar aquesta limitació, hem generat tres models digitals de superfície (MDS) històrics mitjançant fotogrametria d'imatges aèries històriques en dues falles actives de la Serralada Bètica: les falles de Palomares i del Llano del Águila. Hem generat dos MDS per a la Falla de Palomares, un a partir del vol americà sèrie B, 1956–1957, i un del vol interministerial, 1973–1986, i un MDS per a la Falla del Llano del Águila a partir del vol interministerial, tots amb una resolució espacial de 2 × 2 m. Hem introduït la rugositat superficial com una nova mètrica diagnòstica per avaluar la qualitat dels models i identificar-hi els artefactes, mentre que l'anàlisi del model digital de elevacions obtingut de les diferències entre models digitals del terreny s'han utilitzat per quantificar els canvis d'elevació i avaluar la consistència de les superfícies reconstruïdes. En comptes de centrar-nos exclusivament en la precisió absoluta de la geolocalització, el nostre enfocament posa l'èmfasi en l'avaluació de la fiabilitat de la reconstrucció de la superfície històrica. Aquesta metodologia mostra el potencial de les imatges aèries històriques per millorar la caracterització de falles actives i les anàlisis morfotectòniques prop de les falles en paisatges fortament modificats per l'activitat humana.

Paraules clau: Fotogrametria. Imatges aèries històriques. Estudis de falles actives. Rugositat superficial. Modificació antropogènica del paisatge. Falla de Palomares. Falla del Llano del Águila.

Modelos digitales de superficie derivados de imágenes aéreas históricas en áreas altamente antropizadas aplicados al estudio de fallas activas (Béticas orientales, España)

Resumen

El reconocimiento de formas del relieve y el análisis de la superficie son fundamentales en los estudios geomorfológicos y morfotectónicos. En particular, el estudio detallado de la expresión superficial de las fallas activas es esencial para su caracterización como fuentes sísmicas en modelos de peligrosidad sísmica basados en fallas. Sin embargo, la creciente acción antropogénica ha alterado de manera profunda el paisaje natural, degradando o eliminando las formas tectónicas y limitando la caracterización precisa de las fallas activas en muchas regiones del mundo.

Un ejemplo paradigmático lo constituye el sureste de la Península Ibérica, donde el intenso desarrollo agrícola de las últimas décadas ha transformado completamente el paisaje natural. Para abordar esta limitación, se han generado tres modelos digitales de superficie (MDS) históricos mediante fotogrametría a partir de imágenes aéreas históricas en dos fallas activas de la Cordillera Bética: las fallas de Palomares y del Llano del Águila. Se elaboraron dos MDS para la Falla de Palomares, uno a partir del vuelo americano serie B, 1956–1957, y otro del Vuelo Interministerial, 1973–1986), y un MDS para la Falla del Llano del Águila a partir del Vuelo Interministerial, todos con una resolución espacial de 2 × 2 m.

Se introduce la rugosidad superficial como una nueva métrica diagnóstica para evaluar la calidad de los modelos e identificar artefactos, mientras que los análisis de diferencias entre modelos digitales de elevación (MDE) se utilizaron para cuantificar los cambios de elevación y evaluar la consistencia de las superficies reconstruidas. En lugar de centrarse únicamente en la precisión absoluta de la geolocalización, el enfoque propuesto pone el énfasis en la evaluación de la fiabilidad de la reconstrucción de la superficie histórica. Esta metodología pone de relieve el potencial de las imágenes aéreas históricas para mejorar la caracterización de fallas activas y los análisis morfotectónicos en las proximidades de las fallas en paisajes fuertemente modificados por la actividad antropogénica.

Palabras clave: Fotogrametría. Imágenes aéreas históricas. Estudios de fallas activas. Rugosidad superficial. Modificación antropogénica del paisaje. Falla de Palomares. Falla del Llano del Águila.